Svein Jonsson Brennhaug

Synthesis and Carboxyl-Functionalization of Iron Oxide Nanoparticles for Diagnostics

Master’s thesis in Chemical Engineering and Biotechnology
Supervisor: Sulalit Bandyopadhyay
Co-supervisor: Nesrine Bali
July 2022

Master’s thesis

NTNU
Norwegian University of Science and Technology
Faculty of Natural Sciences
Department of Chemical Engineering

NTNU
Norwegian University of
Science and Technology

Svein Jonsson Brennhaug

Synthesis and Carboxyl-Functionalization of Iron Oxide Nanoparticles for Diagnostics

Master's thesis in Chemical Engineering and Biotechnology
Supervisor: Sulalit Bandyopadhyay
Co-supervisor: Nesrine Bali
July 2022

Norwegian University of Science and Technology
Faculty of Natural Sciences
Department of Chemical Engineering

NTNU
Norwegian University of
Science and Technology

Abstract

Investigation and research of iron oxide nanoparticles (IONPs) have experienced rapid growth over the last decades due to their vast potential applications within multiple fields, such as biomedicine, water treatment and catalysis. One of the many superior properties is the great magnetism exhibited, which, combined with functionalizing the nanoparticles with polymers that can bind biomolecules, enables the possibility of rapidly extracting targeted biomolecules using magnetic separation. An example of such a polymer is poly(acrylic acid) (PAA) which by coating provides free carboxyl groups on the surface of the nanoparticles. Multiple groups have previously reported PAA-coating of IONPs synthesized by coprecipitation, but there are few studies on using IONPs synthesized by thermal decomposition for this purpose.

In this thesis, several methods for synthesizing IONPs by thermal decomposition were looked into. A selection of the obtained nanoparticles was either transferred from organic to aqueous phase or coated with PAA to provide free carboxylic groups on the surface of the nanoparticles. Characterizing the functionalized IONPs showed that PAA-coating gave the highest amount of carboxylic group on the surface compared to carboxyl-functionalization by phase transfer. Still, the demonstration of using the IONPs in nucleic acid extraction showed good performance regardless of the number of carboxyl groups. Compared to PAA-coated IONPs synthesized by coprecipitation, two of the proposed carboxyl-functionalized IONPs showed the same level of performance.

All the functionalized IONPs exhibited superparamagnetic properties at room temperature, and the most promising method gave saturation magnetization at 76 emu/g. For further studies, it is proposed to look into how the size and carboxylic content on cubic-shaped IONPs can be optimized to fit specific applications in diagnostics.

Sammendrag

De siste tiårene har det vært en kraftig økning i omfanget av forskning på nanopartikler av jernoksid, på grunn av dets anvendelse i flere potensielle applikasjoner innenfor ulike fagfelt, som blant annet biomedisin, vannbehandling og katalyse. En av de mange overlegne egenskapene er høy magnetisme, hvilket kombinert med funksjonalisering av nanopartiklene med polymere som kan binde biomolekyler, åpner opp for muligheten av rask og målrettet ekstrahering av biomolekyler ved magnetisk separasjon. Et eksempel på en slik polymer er poly(akrylsyre) (PAA) som ved belegning sørger for frie karboksylgrupper på overflaten av nanopartiklene. Flere grupper har tidligere rapportert PAA-belegning av jernoksid nanopartikler som er syntetisert ved samutfelling, men det finnes få studier hvor jernoksid nanopartikler syntetisert ved termisk nedbryting er benyttet til dette formålet.

I denne avhandlingen ble det studert flere metoder for å syntetisere jernoksid nanopartikler ved termisk nedbrytning. Et utvalg av disse ble enten overført fra organisk til vandig fase eller belagt med PAA for å skaffe frie karboksylgrupper på overflaten av nanopartiklene. Karakterisering av de funksjonaliserte jernoksid nanopartiklene viste at PAA-belegning gav størst mengde av karboksylgrupper på overflaten sammenlignet med karboksylfunksjonalisering ved faseoverføring. Likevel viste demonstrasjonen av anvendelse av jernoksid nanopartiklene til ekstraksjon av nukleinsyre, at prestasjonen var uavhengig av antall karboksylgrupper. Sammenlignet med PAA-belagte jernoksid nanopartikler syntetisert ved samutfelling, utviste to av de foreslåtte karboksylfunksjonaliserte jernoksid nanopartiklene prestasjon på samme nivå.

Alle de funksjonaliserte jernoksid nanopartiklene utviste superparamagnetiske egenskaper ved romtemperatur, hvor den mest lovende metoden ga magnetisk metning på 76 emu/g. For videre arbeid foreslås det å se videre på hvordan størrelse og mengde av karboksylgrupper på kubiske jernoksid nanopartikler kan

optimaliseres for å tilpasses spesifikke applikasjoner innenfor diagnostikk.

Preface

This thesis was written in the spring of 2022, and completes my MSc. in Chemical Engineering at the Norwegian University of Science and Technology.

First of all, I want to thank and express my deepest gratitude to my supervisor, Associate Professor Sulalit Bandyopadhyay, for giving me the opportunity to work on this project and for showing me the true meaning of dedication. Although his schedule has been full, he have always made time for helping me out whenever that have been necessary. He has also shown the utmost patience and motivated me throughout this project, for that I am forever grateful.

I also want to thank my co-supervisor Nesrine Bali for her kind words and all of our interesting conversations, as well as the many insightful ideas. She has been rooting for me all the way, and I'm grateful that I got to know her.

Thanks to the engineers at the Particle Engineering Core, NTNU NanoLab and CMIC for your help and support. And a thanks to all the nice people in the Particle Engineering Research Team for the warm and supporting environment. It has been a pleasure to get to know you all.

I would like to thank my friends and fellow students at my study program. I am left with so many memories from the five years we have spent together, and I will cherish them forever.

Lastly, I would like to thank my family for always believing in me and giving me the moral support to finish my degree. The unconditional love that I get from them every day means everything to me.

Contents

Figures

Tables

Chapter 1

Introduction

Nanotechnology and nanoscience have long been of interest to scientists worldwide, and in the last decades, there has been an exponential growth of research in the field. As more knowledge and apparatus are available, the limit of what can be studied is pushed. The reason for this interest is the extraordinary properties that come to show when moving from the bulk materials down to the nanoscale, which also offers the possibility to tune these properties to fit specific applications. When entering the nanoscale, the principles of classical physics are no longer considered sufficient, and the principles of quantum mechanics are governing. [1] Depending on the material, the nanomaterial could possess utterly different chemical, optical, electrical and magnetic properties compared to the bulk material.

1.1 Motivation

A nanomaterial that has gained tremendous interest is iron oxide nanoparticles (IONPs) due to their high surface-to-volume ratio, superparamagnetic properties and biocompatibility. A large number of facile methods for synthesizing IONPs are reported, many of which offer the possibility of tuning the size, shape and magnetic property of the obtained particles. This has led to IONPs being used in a wide range of applications, such as biomedicine, catalysis and water treatment. [2] For this thesis, the focus has been on fabricating IONPs for application in diagnostics and more specific nucleic acid extraction. Previous work by the group has shown the great potential of using poly(acrylic acid) (PAA) to coat IONPs synthesized by coprecipitation for this purpose. PAA offers the possibility of having carboxylic groups on the surface of the IONPs, which then would bind to nucleic acid such as RNA or DNA. Concerning applications, this would lead to a more rapid preparation of samples that are to be biologically tested, as the extraction can be done by placing the sample to a magnet. The nucleic acids bound to the IONPs would then attach to the magnet and can be separated from the rest of the solution.

A disadvantage of using IONPs synthesized by coprecipitation is that the fabricated IONPs have a lower monodispersity than compared to IONPs synthesized by thermal decomposition. It is not known how this affects the polymer coating, as the mechanism behind this is still to be uncovered. Using thermal decomposition improves the monodispersity and it is also possible to tune both the size and the shape of the IONPs. Another advantage is that the saturation magnetization can be improved as well, depending on the synthesis route, which enhances the rapid extraction. The aim of this thesis is therefore to investigate different methods to synthesize IONPs by thermal decomposition, that are to be functionalized with carboxylic groups and eventually tested in application. Based on the results it would be evaluated if any of the methods can be proposed as alternative to the already established procedure with coprecipitated IONPs.

1.2 Outline

The thesis consist of five chapters. The first chapter is the introduction where the motivation behind this study is presented. Moving on to chapter two the theoretical background on crystallization theory and synthesis of IONPs is presented. Chapter three presents the materials and methods used for this study. In the fourth chapter the results from the experimental work will be presented and discussed, before a final conclusion is given in chapter five. A suggestion for further studies is also presented in the last chapter.

Chapter 2

Theoretical Background

For the synthesis of nanomaterials there are numerous methods, and which method is chosen is based upon the desirable product and use. It is common to split these methods into two categories; top-down and bottom-up approach. In the top-down approach larger materials are broken down into smaller dimensions, whereas for bottom-down the nanomaterials are build up from atomic or molecular scale into higher complex nanoscale assembly. [1] Further in this chapter the latter will be further discussed.

2.1 Crystallization

A commonly used bottom-up approach for synthesizing nanoparticles in solution is crystallization. The main concept is to induce a phase transition from a disorded state to a crystal phase, and thereby reducing the high free energy to a favorable low free energy state. [3] Crystallization can be split into two main events; nucleation and growth.

2.1.1 Supersaturation

To be able to understand why nucleation happens, it is crucial to establish the concept of supersaturation. In loose terms supersaturation can be described as dissolving a solid in solution in such an amount that the concentration goes above the solubility limit. This can be achieved by applying different processes to the system. For instance, if the solubility of a specie increases with increasing temperature, the specie can be dissolved at elevated temperature before bringing the system to a lower temperature. The solution will then be supersatured and go into a state referred to as a metastable zone. It is first when the system is in this metastable zone that crystallization can occur. Increasing the supersaturation even more brings the system into the labile zone. However it is unusual to do this as this will cause problems with trying to control the precipitation.

In classical nucleation theory, CNT, this concentration-based understanding of supersaturation comes in short, and an activity-based supersaturation is employed. This is obtained by first establishing the driving force for crystallization, which is the change in chemical potential from the dissolved substance (state 1) and the crystal (state 2). [1]

$$\Delta\mu = \mu_1 - \mu_2 \tag{2.1}$$

The formula for chemical potential is as follows:

$$\mu = \mu_0 + RT \ln a, \tag{2.2}$$

where the μ and μ_0 is the chemical potential and the standard potential respectively, and a is the activity. R and T is the temperature and the universal gas constant. The activity is further defined in terms of concentration of a solute (C) as;

$$a = C\gamma. \tag{2.3}$$

The γ, or the activity coefficient for an ideal solution is equal to one. However for a non-ideal solution the activity coefficient takes into account the ionic strength of the solution, charge and size of each component due to the interactions between chemical species. Together with the concentration this makes up the activity and it becomes a measure of the effective concentration in the solution.

These equations make together up the following relation:

$$\Delta\mu = RT \ln\left(\frac{a}{a^*}\right), \tag{2.4}$$

where a is the activity in an arbitrary state and a^* is the activity at equilibrium. It is this ratio that is defined as the supersaturation, S, and it tells how likely it is for the system to precipitate. In order for a crystallization to happen spontaneously $\Delta\mu$ must be greater than zero, hence $S > 1$.

2.1.2 Nucleation

Nucleation can be described as the birth of a new phase in the solution. This requires that the supersaturation is established, and thereby the driving force for crystallization. When working with larger sized particles, such as particles in the micron size range, it is common to separate between primary and secondary nucleation due to shear forces being active on the particles. This is not relevant for nanoparticles, and secondary nucleation will not be discussed further.

Primary nucleation can be either homogeneous or heterogeneous. [4] The difference between these is whether the nucleation happens spontaneous or if a solid surface is present and induces the nucleation. Both mechanisms will be discussed further.

Primary homogeneous nucleation

It is already establish that solutes crystallizes due to reduction in free energy, this will be elaborated further here. In primary nucleation nucleation occurs spontaneously. [5] Then total Gibbs free energy change, ΔG can be expressed as:

$$\Delta G = \Delta G_v + \Delta G_s, \tag{2.5}$$

where ΔG_v is the free energy change for the phase transition and ΔG_s is the free energy change for the formation of a surface. In Figure 2.1 it is shown how the two terms on the right hand side of Equation 2.5 changes the free energy in the system as a function of radius for a spherical nucleus. The former term is contributing to a negative change and decreasing proportional with the volume of the crystallite, and represents the excess free energy of the metastable solution over the solid deposition. The latter term however is increasing proportional with the surface area of the crystallite, and represents the energy cost of forming a solid-liquid interface. Equation 2.5 can be rewritten with respect to the volume, V, and surface, A of the nucleus as:

$$\Delta G = V\Delta G_v + A\gamma \tag{2.6}$$

γ is the interfacial tension that arises between the forming crystalline surface and solution. For a spherical nucleus with a given radius r, the equation is extended to:

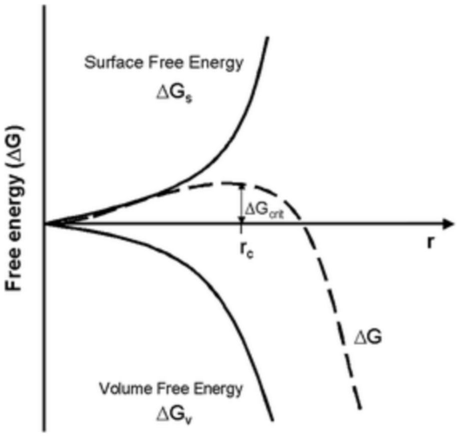

Figure 2.1: The change of free energy as a function of radius for a spherical nucleus.[6]

$$\Delta G = \frac{4}{3}\pi r^3 \Delta G_v + 4\pi r^2 \gamma \tag{2.7}$$

As seen in Figure 2.1 ΔG would increase for nuclei with small radius, as the energy cost of creating a surface is higher than the excess free energy that comes from the deposition of a crystallite. This overall increase in the free energy is not energetically favorable and a stable nucleus can not be formed. At one point the radius will reach a critical size, r^* where the excess free energy surpasses the surface free energy and stable nuclei can be formed due to a decrease in the overall free energy. This can be shown mathematically by looking at the derivative of Equation 2.7.

$$\frac{\Delta G}{dr} = 4\pi r^3 \Delta G_v + 8\pi r \gamma = 0 \tag{2.8}$$

$$r^* = -\frac{2\gamma}{\Delta G_v} \tag{2.9}$$

Further ΔG_v can be defined in terms of supersaturation and Boltzmann constant, k_B.

$$\Delta G_v = -\frac{v k_B T \ln S}{v_m} \tag{2.10}$$

Combining Equation 2.7, 2.9 and 2.10 gives the expression for the critical energy barrier that must be overcome in order to form a stable spherical nucleus.

From this expression it can be observed that temperature, supersaturation and interfacial energy are important parameters for primary homogeneous nucleation.

$$\Delta G^* = \frac{16\pi\gamma^3}{3\Delta G_v^2} = \frac{16\pi\gamma^3 v_m^2}{3k_B^3 T^3 (v \ln S)^2} \tag{2.11}$$

Primary heterogeneous nucleation

The main difference between homogeneous and heterogeneous nucleation is the presence of a substrate surface where the nucleation can take place for heterogeneous nucleation. The thermodynamically expressions for critical size and energy barrier still holds with some modifications. Since the nucleus can sit on a surface the interfacial free energy is somewhat reduced, compared to the interfacial energy that arises for the crystal in contact with the solution. How much this is reduced depends on the contact angle, θ, between the nucleus and substrate. [3] Young's equation is used to describe the interfacial tension, as given in Equation 2.12.

$$\gamma_{ns} + \gamma_{nl} \cos\theta = \gamma_{sl} \tag{2.12}$$

The lower the value of contact angle, the more is the energy barrier reduced. Figure 2.2 shows three scenarios: $\theta < 90°$, $90° < \theta < 180°$ and $\theta = 180°$. The first shows a favorable nucleus-surface interactions, whereas the second is unfavorable. For the third there is no interaction, hence no reduction in the energy barrier. This relation can be described by introducing a factor, ϕ, that relates the contact angle and energy barrier reduction with the energy barrier for homogeneous nucleation.

$$\Delta G^*_{\text{het}} = \phi \Delta G^*_{\text{hom}} = \left(\frac{(2+\cos\theta)(1-\cos\theta)^2}{4} \right) \Delta G^*_{\text{hom}} \tag{2.13}$$

By having the contact angle at 180° Equation 2.13 gives $\Delta G^*_{\text{het}} = \Delta G^*_{\text{hom}}$.

2.1.3 Growth

After the supersaturation is established and nucleation has begun, the last step towards formation of nanoparticles remains, namely the crystal growth. The growth is what mainly consumes the rest of the supersaturation, after a certain amount of nuclei is formed. The fundamental driving force for growth to occur is the same

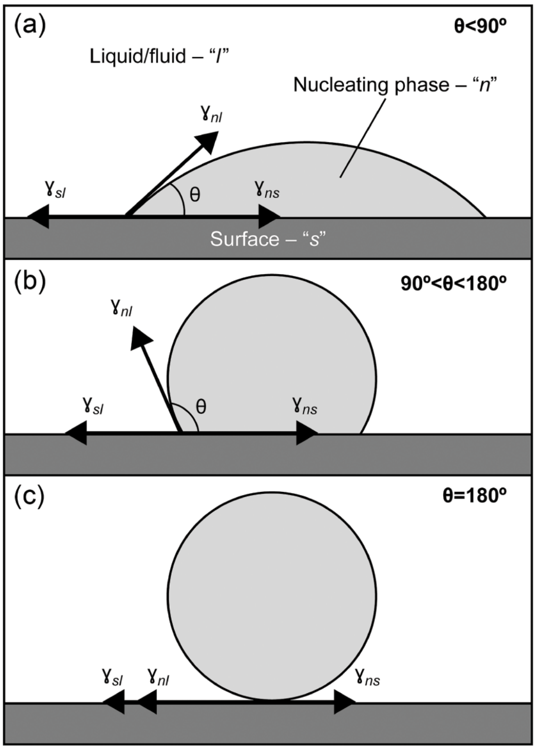

Figure 2.2: Illustration of the equilibrium descibed by Young's equation.[7]

as for nucleation, to reduce the free energy in the system. In short terms crystal growth can be defined as size enlargement of crystalline particles by monomer addition. This enlargement process is what determines the final size and morphology of the particles. It is therefore crucial to understand and control the crystal growth when aiming for size and shape tuning of particles.

In solution crystal growth can be seen as dynamic process of attachment and detachment of monomers, the building units, on to the surface of the crystal and incorporation into the lattice sites. So there are two main processes that occurs. Firstly is the transportation of monomers from the solution to the crystal surface, and secondly it is the incorporation of the units into the crystal lattice. The former is a diffusion-controlled mechanism, whereas the latter is reaction-controlled. Which mechanism that is the most dominant can be determined by the growth order, g, which again comes from the growth rate law: [8]

$$R = k(S-1)^g, \tag{2.14}$$

where R is the growth rate and k is the growth rate constant. If $g = 1$ the

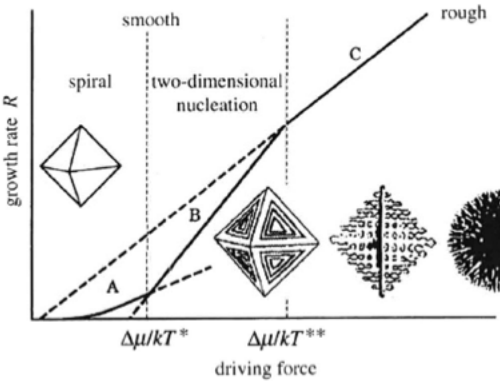

Figure 2.3: Growth rate as a function of driving force. [8]

growth mechanism is mainly diffusion-controlled and gives rise to what is referred to as rough growth. This is due to a very high level of supersaturation, which yields a large amount of active sites on the surface and the incorporation of of monomers into the lattice happens rapid. It is therefore the transportation of monomers by diffusion that limits the growth, hence diffusion-controlled. When the supersaturation is lower, the mechanism changes to reaction-controlled. Then at low supersaturation and $g = 2$ spiral growth is obtained, whereas a moderate level of supersaturation and $g > 2$ yields polynuclear growth or two-dimensional nucleation. In Figure 2.3 the three different type of growths are presented as a function of driving force, i.e. supersaturation.

2.2 Iron Oxide Nanoparticles

The last decades nanoparticles of iron oxide has received tremendous attention, due to its large extent of potential applications in e.g. biomedicine and water treatment. However, iron oxide is not something new. It exist in many phases in the nature, whereas rust might be the one most are familiar with. To this day there are 16 different phases of iron oxide that has been identified, where magnetite (Fe_3O_4), maghemite (γ-Fe_2O_3) and hematite (α-Fe_2O_3) are the most common ones. [2]

There are several properties that make iron oxide nanoparticles (IONPs) excellent candidates for use in biomedical applications. They are biocompatible and exhibit higher chemical stability compared to other similar nanoparticles, and furthermore they possess unique magnetic properties such as superparamagnetism and high saturation magnetization. This makes them suitable for use in magnetic resonance imaging (MRI) as contrast agents, cell separation and detection, treatment for hyperthermia and drug delivery. [9][10][2]

Regarding the synthesis of IONPs there are multiple synthetic routes. Among these the most common is coprecipitation, microemulsion, and thermal decomposition. [11] All the synthetic routes have both advantages and disadvantages. Coprecipitation is a relatively simple and cost-effective method, but the synthesized IONPs tend to have a broad size distribution and aggregation occurs in a greater extent. In addition the crystallinity is often poor. If size control is desirable microemulsion is a suitable method. However, the yield of the syntheses are quite low compared to other methods, and it takes a lot of time. Lastly, thermal decomposition offers the possibility to tune both size and shape of the synthesized IONPs. The greatest challenge with IONPs synthesized by thermal decomposition is that they often are hydrophobic and only dispersible in non-polar organic solvents. To overcome this, phase transfer from organic to aqeous phase is necessary. [12]

2.2.1 Thermal decomposition

High-temperature thermal decomposition offers the possibility of synthesizing highly crystalline nanoparticles with a narrow size distribution and high monodispersity. A typical method involves an organometallic precursor, such as iron acetylacetonate ($Fe(acac)_3$) or iron pentacarbonyl ($Fe(CO)_5$), an organic solvent, and one or multiple surfactants. The LaMer model by *V. LaMer* and *R. Dinegar*, shown in Figure 2.4, can be applied to describe what is happening within the reaction environment. [13] At high temperature the precursor will start to decompose into smaller units, or monomers, referred to as the decomposition temperature. Over time the concentration of free monomers in the solution will increase and eventually it surpasses the supersaturation threshold. This initiates the nucleation process to happen and nuclei are starting to form, which consumes much of the free monomers. Consequently, the concentration decreases and go below the supersaturation threshold. Further nucleation is prevented and the reaction goes into the growth regime. The formed nuclei will continue to grow until the concentration of free monomers reaches the solubility limit. Eventually Ostwald ripening can occur, this is a phenomena where smaller particles below a critical size will redissolve into the solution again and larger particles will use the monomers to grow. [14]

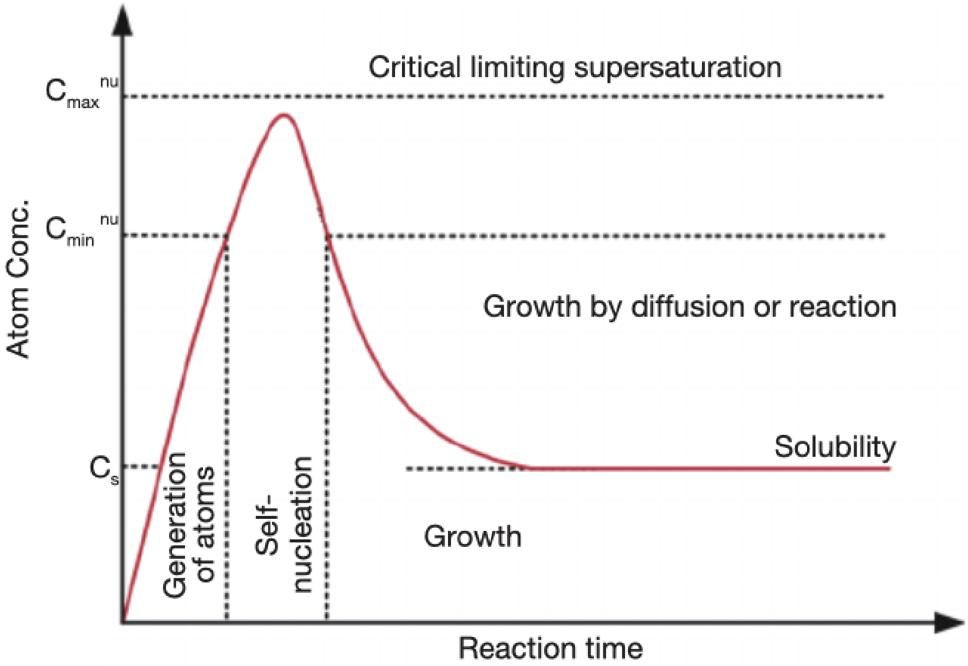

Figure 2.4: The LaMer model proposed by *V. LaMer* and *R. Dinegar*. Schematic illustration is obtained from *Y. Chen et al.*[15]

Chapter 3

Methodology

In the following chapter, the experimental methods for the syntheses will be presented, as well as preparation and conduction of the characterization techniques that has been carried out for the thesis.

3.1 Materials

Iron(III) chloride hexahydrate ($FeCl_3 \cdot 6\,H_2O$), iron(0) pentacarbonyl ($Fe(CO)_5$), 1-octadecene (ODE, technical grade, 90%), didecyldimethylammonium bromide (DDAB, 98%), iron(III) acetylacetonate ($Fe(acac)_3$), benzyl ether (BE, 98%), oleic acid (OA, technical grade, 90%), 1,2-hexadecanediol (HDD, technical grade, 90%), oleylamine (OAm, technical grade, 70%), tri(ethylene glycol) (TREG, 99%), ethyl acetate (99.5%), sodium dodecyl sulfate (SDS), potassium persulfate (KPS) and acrylic acid (AA) was obtained from Merck Life Science/Sigma-Aldrich Norway AS. Sodium oleate (97%) was purchased through VWR. MilliQ water was used throughout the experiments.

3.2 Synthesis of IONPs

3.2.1 Thermal decomposition of $Fe(CO)_5$ + DDAB

Core-shell IONPs were prepared following a method previously reported by *G. Singh et al.* [16] For the synthesis the setup shown in Figure 3.1 was used. In the three-neck round bottom flask 25 mL of ODE and 325 mg didecyldimethylammonium bromide (DDAB, 0.8 mmol) was added. The solution was magnetically stirred at 700 rpm and degassed at 120 °C under argon atmosphere for 30 minutes. After degassing the temperature was raised to 180 °C and 1.4 mL of the precursor iron pentacarbonyl ($Fe(CO)_5$, 10.36 mmol), was injected through the septa to maintain the inert atmosphere and avoid air exposure of the precursor. The reaction was maintained at this temperature for 30 minutes, before the temperature was raised to 220 °C with a rate of 20 °C/min and kept at this temperature for two hours. The solution was cooled down to room temperature, and the magnetic stir bar was washed with hexane. Acetone was added to precipitate the particles, which was magnetically separated, and the supernatant was discarded. The NPs were washed twice by redispering the NPs in hexane, and precipitated again with acetone. Toluene was used as dispersion medium for long-term storage.

3.2.2 Thermal decompostion of $Fe(CO)_5$ + OAm

Core-shell IONPs were prepared following a method reported by *S. Peng et al.* [17] In a three-neck round bottom flask 50 mL of ODE and 740 μL OAm was added, and degassed under an argon blanket at 120 °C for 30 min. The magnetic stirring was set to 700 rpm during the entire synthesis. After degassing the temperature was raised to 180 °C. Once the temperature was stable 1.8 mL of $Fe(CO)_5$ was injected into the hot solution through a septa. The reaction temperature was maintained for another 20 minutes, before allowing the solution to cool down to room temperature. Once cooled down, the supernatant was discarded and nanoparticles were washed off the magnet using 20 mL hexane. Acetone was added to precipitate the nanoparticles, which were further separated from the solution using a magnet. The obtained particles were washed another two times with acetone and hexane, before re-dispering in toluene for long-term storage.

3.2.3 Thermal decomposition of $Fe(acac)_3$ + TREG

Water-soluble IONPs were synthesized following a modified method reported by *Maity et al.* [18] The synthesis took place using the standard thermal decomposition setup, as shown in Figure. Briefly, 706 mg (2 mmol) of $Fe(acac)_3$ was dissolved in 20 mL of TREG in a three-neck round bottom flask. The reaction mixture was magnetically stirred under an argon blanket at 400 rpm. Degassing was carried out at 120 °C for one hour before raising the temperature to 280 °C for another two hours. After cooling the reaction mixture to room temperature, 20

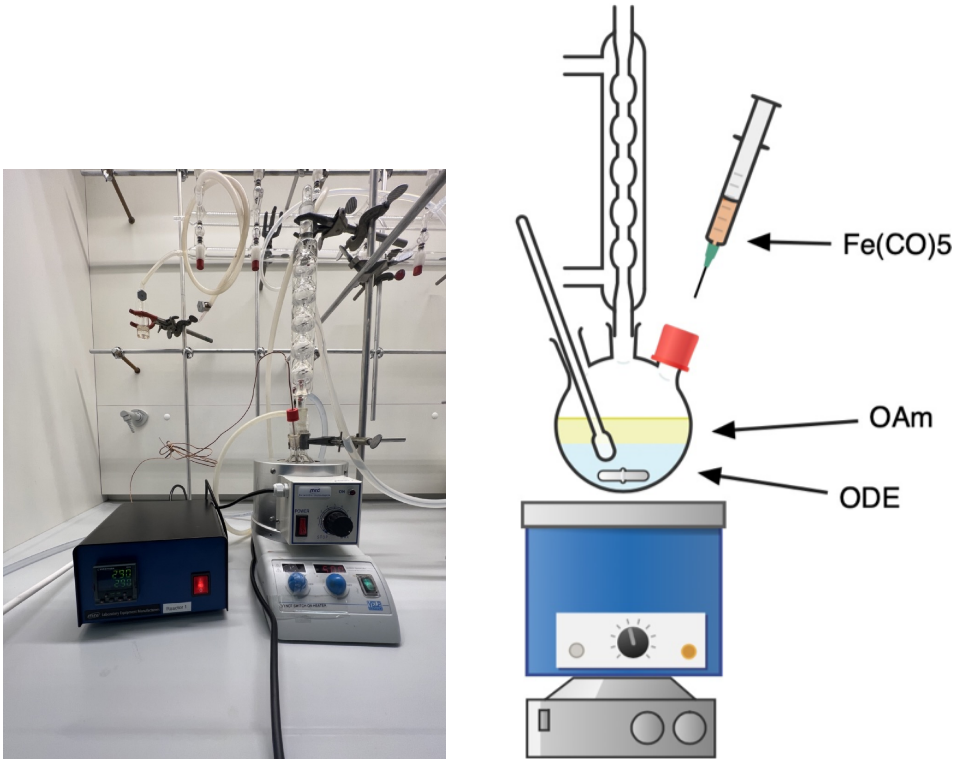

Figure 3.1: Image of the thermal decomposition setup and a schematic illustration of the synthesis with $Fe(CO)_5$, OAm and ODE.

mL of ethyl acetate was added to the solution to precipitate the nanoparticles, which were further separated using a magnet. Ethanol was added for redispersion. The washing procedure was repeated three times before redispersing the nanoparticles in water for long-term storage.

3.2.4 Thermal decomposition of $Fe(acac)_3$ + OAm

The protocol for the synthesis was adapted from the work of *Z. Xu et al.* [19] In the three-neck round bottom flask 3 mmol of $Fe(acac)_3$ was dissolved in a mixture of 20 mL OAm and 10 mL BE. The round bottom flask was connected to a temperature controller and the Schlenk line through a condenser as shown in Figure 3.1. After degassing the reaction at 110 °C for one hour under nitrogen atmosphere, the reaction temperature was raised to 300 °C with a heating rate of 20 °/min. The reaction was refluxed for one hour, before it was cooled down to room temperature. IONPs were washed thrice with 50 mL ethanol and magnetically separated. For long-term storage, the IONPs were dispersed in toluene.

3.2.5 Thermal decomposition of $Fe(acac)_3$ + OA

Cubic-shaped IONPs were synthesized following a method extracted from the work of *G. Singh et al.* [20] The reaction was carried out at *NTNU NanoLab* as it was necessary to have a vacuum pump connected to the Schlenk line. The setup can be seen in Figure 3.2. In a three-neck round bottom flask connected to a temperature controller, condenser and vacuum Schlenk line, 0.71 g $Fe(acac)_3$ (2 mmol) and 1.26 mL OA (4.2 mmol) was dissolved in 20 mL BE. The reaction mixture was degassed at 100 ° for one hour with applied vacuum at 0.02 mbar. After the degassing, vacuum was turned off and argon was flushed into the reaction environment to maintain inert atmosphere. With a heating rate of 20 °/min the reaction was brought up to reflux at 290 °C, and maintained at reflux for 30 minutes. The solution was cooled down to room temperature, before a mixture of 40 mL toluene and 10 mL isopropanol was added to precipitate the IONPs. The IONPs were magnetically separated and the supernatant was discarded. Washing of the IONPs were done thrice with a mixture of 20 mL acetone and 10 mL hexane, before redispering in toluene for long-term storage.

3.2.6 Thermal decomposition of $Fe(acac)_3$ + OA/OAm/HDD

The synthesis of cubic-shaped IONPs was extracted from the work of *H. Yang et al.*, and the reaction was carried out using the setup shown in Figure 3.1. [21] In a three-neck round bottom flask 0.3 g $Fe(acac)_3$ (1 mmol) and 2.1 g HDD (8 mmol) was dissolved in a mixture of 5.08 mL OA (16 mmol), 1.32 mL OAm (4 mmol) and 20 mL BE. Degassing took place for one hour under argon atmosphere at 110 °C, before the temperature was raised to 200 °C. The reaction maintained at this temperature for 30 minutes, and was then brought up to reflux at 290 °C with a heating rate of 15 °C/min. The refluxing was maintained for one hour, before the solution was cooled down to room temperature. The IONPs were magnetically separated and washed thrice with 50 mL ethanol, before redispering in toluene for long-term storage.

3.2.7 Thermal decomposition of FeOleate + OA

FeOleate was prepared by dissolving 5.40 g $FeCl_3 \cdot 6\,H_2O$ and 18.25 g NaOleate in 40 mL EtOH, 30 mL MQ water and 70 mL hexane in 250 mL round bottom flask, which was placed in an oil bath. Magnetic stirring was set 1100 rpm and

Figure 3.2: Setup for thermal decomposition at *NTNU NanoLab*

the solution was refluxed at 70 °C for 4 hour. After the synthesis, the red organic phase was separated from the aqeous phase and washed thrice with MQ water. Lastly, hexane was evaporated at 70 °C by the use of rotary evaporator.

In the three-neck round bottom flask in the setup shown in Figure 3.1, 1.6 g FeOleate and 600 μL OA was dissolved in 25 mL ODE. Under argon atmosphere, the solution was heated up to reflux at 320 °C with a heating rate of 3 °/min. The reaction was kept refluxing for 45 minutes, before the solution was cooled down to room temperature. The IONPs was precipitated with a mixture of hexane and isopropanol, and magnetically separated. The supernatant was discarded, and the IONPs was further washed thrice with acetone and finally redispersed in toluene for long-term storage.

3.3 Phase transfer and carboxyl-functionalization

3.3.1 Base-bath-assisted phase transfer

For the phase transfer of hydrophobic OAm-capped IONPs, a modified protocol based on the work of *V. Vilas-Boas et al.* was conducted. [22] In a centrifuge tube 5 mL of IONPs dispersed in toluene (10 mg/mL) was mixed with a alkaline solution (20 mL isopropanol + 20 mL MQ water + 2 g KOH). The centrifuge tube was placed in an ultrasonication bath and sonicated for 30 min. Every five minutes, the mixture was vortexed for 15 seconds. After sonication, the mixture was left shaking at 750 rpm for 24 hours. The as-transferred was magnetically separated and washed thrice with ethanol, and twice with MQ-water. For long-term storage the IONPs was redispersed in MQ water.

3.3.2 Phase transfer by oxidative reaction of OA-capped IONPs

This phase transfer was first reported by *J. Cai et al.* [23] In a flask 50 mg IONPs dispersed in 25 mL cyclo-hexane was mixed with 17.5 mL tertiary butanol, 1.25 mL K_2CO_3-solution (5 wt%), 2.5 mL PVP-solution (40 wt%) and 10 mL of oxidizing agent solution (4.5 mg $KMnO_4$ and 225 mg $NaIO_4$). The mixture was magnetically stirred for 2 hours at 700 rpm, as seen in Figure 3.3. The IONPs were extracted from the solution by magnetic separation and washed thrice with ethanol, and twice with MQ water. For long-term storage, the IONPs were dispersed in water.

3.3.3 Coating of IONPs with PAA

PAA-coating of IONPs were conducted using the setup shown in Figure 3.4. In a two-neck round bottom flask, 115 mg SDS was dissolved in 20 mL MQ water. The flask was placed in a oil bath, and magnetic stirring was set to 700 rpm. The solution was degassed with nitrogen for ten minutes, before 166 mg IONPs was added and the temperature was raised to 70 °C. Once the temperature stabilized, 77 μL AA was added and the reaction was allowed to equilibrate for 45 minutes. 200 mg KPS was dissolved in 4 mL MQ water and introduced to the reaction mixture. The polymerization was carried out for 2 hours, keeping the temperature constant at 70 °C, before cooling down the solution to room temperature. The IONPs was then washed thrice with 20 mL MQ water and magnetically separated.

Figure 3.3: Image from the phase transfer of hydrophobic OA-capped IONPs.

The final products were redispersed in 10 mL MQ water.

3.4 Characterization

3.4.1 Quantification of COOH groups

In order to determine the amount of carboxylic groups on the surface of IONPs, a colorimetric method reported by *A. Hennig et al.* was conducted. [24] A HEPES buffer solution was prepared by dissolving 2.38 g of HEPES in 1 L of MQ water, and a 0.2 mM $NiCl_2$ solution was prepared by dissolving 23.77 mg of $NiCl_2 \cdot 6\,H_2O$ in the HEPES buffer solution. 5 mM pyrocatechol violet (PV) was prepared by dissolving 19.32 mg of PV in 10 mL of HEPES buffer solution.

In Eppendorf tubes the samples were prepared by adding 0.2 mg and 0.4 mg IONPs. Triplicates were done for each of the weights. Depending on the concentration of the IONPs, the volume of the sample was adjusted by addition of $NiCl_2$ solution to a final volume of 600 μL. The samples was then incubated at 38 °C for 10 minutes.

Meanwhile, a calibration curve was performed on the UV-VIS sprectropho-

Figure 3.4: Setup used for PAA-coating of IONPs.

meter. Samples were prepared in UV-VIS micro cells according to the Table 3.1. This was done in order to be able to quantify the amount of free nickel ions in later samples.

Cell	1	2	3	4	5	6
$NiCl_2$ sol. (μL)	0	100	200	300	400	500
HEPES sol. (μL)	500	400	300	200	100	0
$NiCl_2$ (mmol)	0	0.02	0.04	0.06	0.08	0.1

Table 3.1: Samples prepared for calibration curve on UV-VIS.

After incubation the samples were centrifuged at 14 500 rpm for 15 minutes. 500 μL of the clear supernatant was transferred into UV-VIS micro cells and mixed with 500 μL of the PV solution. The cell was placed within the instrument and measurement of the absorbance curve was carried out. The maximum absorbance between 550 and 650 nm was reported, and by using the calibration curve it was possible to quantify the amount of nickel ions in the supernatant and thereby how much of the nickel that had bound to the IONPs. By assuming that one nickel binds to 2.65 carboxyl groups, the concentration of carboxylic groups in each samples was calculated.

3.4.2 Electron microscopy imaging

To investigate the shape and size of the obtained nanoparticles, imaging by electron microscopy was carried out on Hitachi SU9000 (S(T)EM) located at NTNU NanoLab and Tecnai 12 (TEM) at EMLab at the CMIC core. Samples were prepared by diluting 20 μL of IONPs in 980 μL of solvent in an Eppendorf tube, which was further vortexed for 1 minute, followed by 2 minutes of sonication and finally 1 minute of vortexing again. A drop of the dilution was placed on a copper TEM grid and left for evaporation.

3.4.3 Dynamic light scattering (DLS)

Hydrondyamic size and zeta potential was measured by Anton Paar Litesizer 500 at the Particle Engineering Core. Samples were prepared in Eppendorf tubes by diluting 10 μL of IONPs in 1 mL MQ water. The dilution was further vortexed for 30 seconds and sonicated 1 minute three times, before loading it to the folded capillary cell. Measurements were carried out in triplicates with 10 runs à 10 seconds, unless stated otherwise.

3.4.4 Vibrating sample magnetometer (VSM)

For measurements of magnetic properties vibrating sample magnetometer (VSM) was used. For preparation of the samples, the IONPs were dried at 65 °C for 24 hours. Dried sample was transferred into gel caps, which was attached to the instrument.

Chapter 4

Results and Discussion

In this chapter, the main findings and results from the experimental work conducted will be presented and discussed. The first section covers the results from the syntheses of IONPs by thermal decomposition and the phase transfer methods, followed by the results from the PAA-coating of IONPs. The next sections contain results from the further characterization of the carboxyl-functionalized IONPs, including quantification of carboxylic group on the surface of the NPs as well as the magnetic properties. Lastly, the performance of the functionalized NPs in nucleic acid extraction is presented.

4.1 Synthesis of IONPs

4.1.1 Thermal decomposition of Iron Pentacarbonyl

High temperature decomposition was carried out for iron pentacarbonyl ($Fe(CO)_5$) in 1-octadecene (ODE), and the surfactant that was used was didecyldimethylammonium bromide (DDAB). The amount of the surfactant for the initial synthesis was 1 mmol, as this had previously been reported by *G. Singh et al.* to give core-shell structured nanoparticles with high saturation magnetization at 152 emu/g. [16] However, as can be seen in Figure 4.1 this was not achieved. The nanoparticles were also observed to be unstable in dispersion with both toluene and hexane, meaning that they would precipitate out immediately. A synthesis with 0.8 mmol of DDAB was therefore carried out. This led to formation of well defined spherical nanoparticles with core-shell structure. The colloidal stability was also improved, as the nanoparticles would remain suspended in the dispersion of toluene. Image analysis by in a calculated diameter of 16 ± 1 nm. The size distribution can be seen in Figure 4.2.

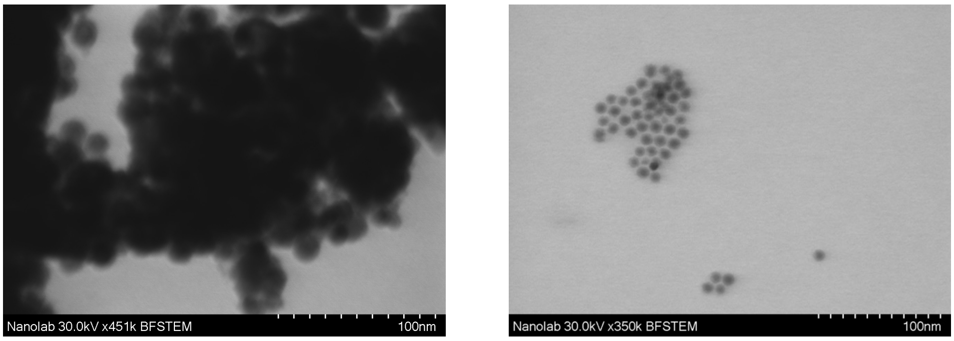

Figure 4.1: BF S(T)EM images of IONPs synthesized by $Fe(CO)_5$ in the presence of 1 mmol (left) and 0.8 mmol DDAB (right).

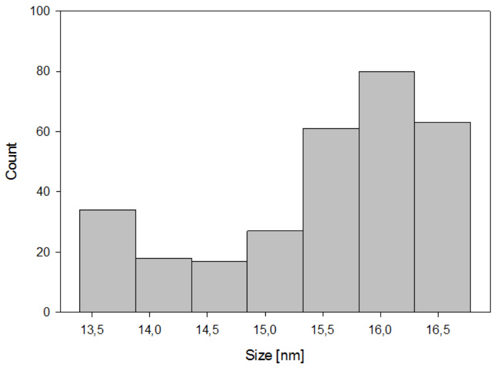

Figure 4.2: Particle size distribution of IONPs prepared by $Fe(CO)_5$ in presence of DDAB (16±1 nm).

Another synthesis with oleylamine (OAm) instead of DDAB as surfactant was also carried out. The modified protocol was extracted from the work of *S. Peng et al.*. [17] The amount of ODE was increased to 50 mL and the amount of OAm was 2.2 mmol. TEM image of the obtained particles are shown in Figure 4.3. As can be observed, spherical shaped particles with a core-shell structure was obtained for this method as well and the size were the same at 16 ± 1 nm. Particle size distribution is shown in Figure 4.4.

The difference between these methods, other than the choice of surfactant, is the heating profile and reaction time. Whereas the synthesis with DDAB had a two hour reaction time, the one with OAm had a reaction time of 20 min only. This is

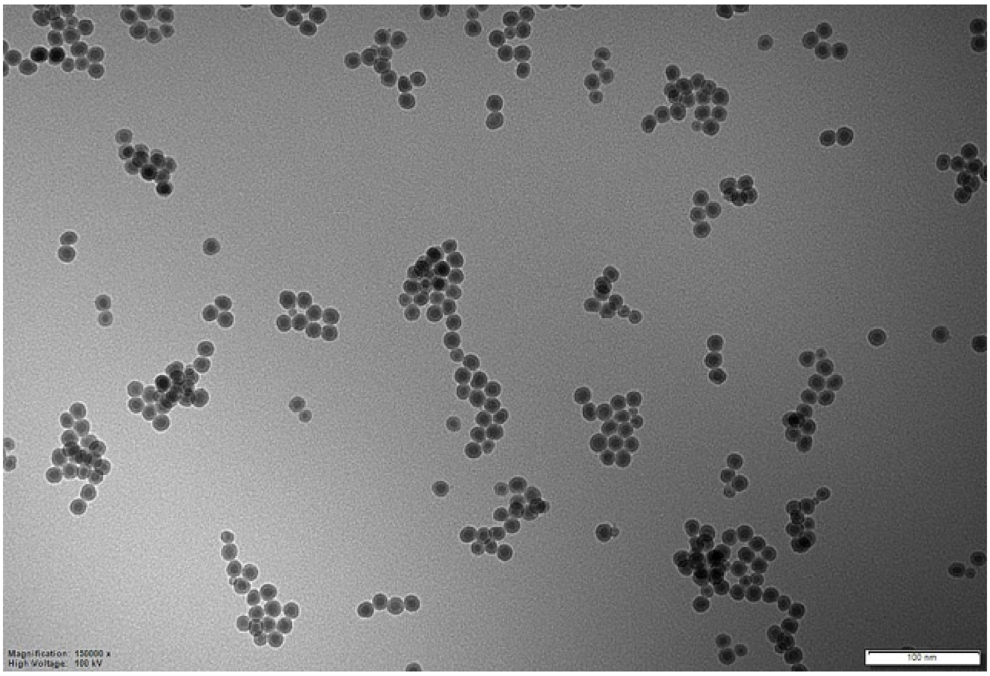

Figure 4.3: TEM image of IONPs synthesized by $Fe(CO)_5$ in the presence of OAm.

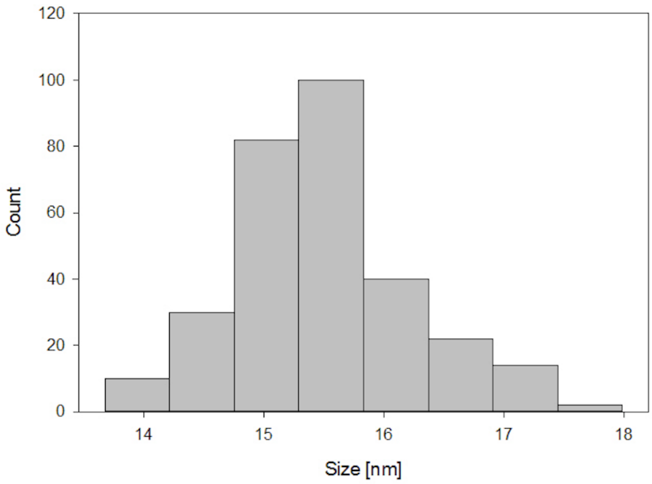

Figure 4.4: Particle size distribution of IONPs prepared by $Fe(CO)_5$ in presence of OAm (16±1 nm)

attributed to a different nucleation rate. After the hot injection of the precursor at 180°C, the bromide ions would form a complex with the precursor, $Fe(CO)_4Br_2$.[16] This leads to a delay in the nucleation as the complex is less reactive than using other typical ligands such as oleic acid and oleylamine, which often form amorphous NPs due to a rapid decomposition. Observations made during the reaction supported this, as the reaction with DDAB had a gradual color change of the reaction mixture from orange to black over a time period of ten minutes, whereas with OAm an almost immediately color change was observed.

4.1.2 $Fe(acac)_3$ + TREG

One disadvantage with preparation of IONPs by thermal decomposition is the formation of hydrophobic nanoparticles, due to use of organic surfactants. Phase transfer is therefore necessary to make the nanoparticles soluble in aqueous solution. It was therefore of interest to find a method which produced hydrophillic nanoparticles. The choice fell on thermal decomposition of $Fe(acac)_3$ in triethylene glycol (TREG), previously reported by *D . Maity et al.* [18] This method differs from the ones mentioned above with it being a one-pot synthesis, meaning that both the precursor and solvent are mixed together from the beginning of the reaction and nothing is added during the synthesis. Whereas for the syntheses with $Fe(CO)_5$, the precursor is added after degassing and at elevated temperature.

S(T)EM image of the obtained particles are shown in Figure 4.5. It was observed that the shape was irregular spherical. The sizes was determined to 8 ± 1 nm. DLS measurements was carried out on Anton Paar Litesizer 500, and samples were prepared as described in Chapter 3.4.3. For measurements of hydrodynamic size each samples were measured three times, and for each measurement there was ten runs à ten seconds, whereas for zeta potential samples were measured in triplicates with 100 runs per measurement. The average hydrodynamic size, polydispersity index and zeta potential with the corresponding standard deviation for all triplicates are given in Table 4.1. These values were directly obtained from the software of the instrument.

Sample	Hydrodynamic size [nm]	Polydispersity index [%]	Zeta potential [mV]
1st batch	291 ± 6	25 ± 1	12.2 ± 0.5
2nd batch	216 ± 15	26 ± 2	13.9 ± 0.4
3rd batch	163 ± 12	25 ± 1	30.9 ± 0.4
4th batch	156 ± 7	25 ± 1	23.5 ± 0.6

Table 4.1: Results from DLS measurements of IONPs synthesized by $Fe(acac)_3$ in the presence of TREG.

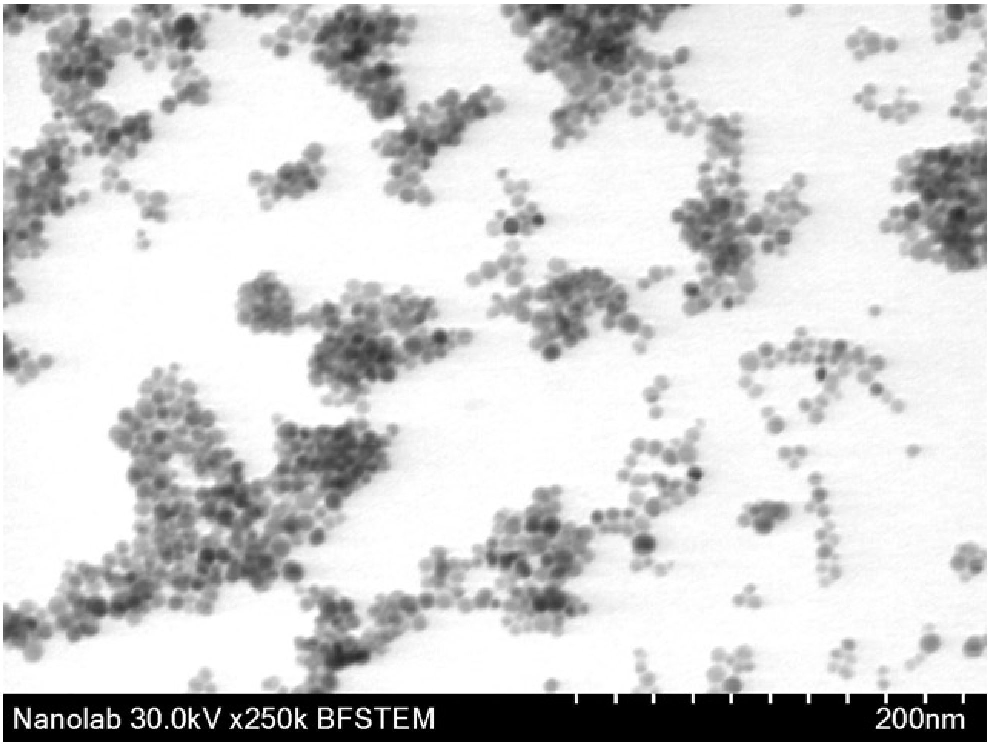

Figure 4.5: BF S(T)EM image of IONPs synthesized by $Fe(acac)_3$ in the presence of TREG.

It was observed that the two first batches had a higher size and lower zeta potential than the last prepared batches. This could be attributed to the effect of washing steps after the synthesis. Initially the number of washing steps was three times with ethyl acetate and ethanol, before redispersing in MQ water. Increasing the number of washings step with ethyl acetate to four, and adding a washing step with only MQ water, reduced the size and increased the zeta potential. There was also tried to redisperse the IONPs in MQ water that filtered through a syringe filter (0.22 μm). This reduced the size of the 4 batch from 156 ± 7 to 122 ± 8 nm, while the zeta potential remained unchanged.

Zeta potential for these particles were reported to have a maximum at around 40 mV. [18] The positive value is explained by the polarization of TREG molecules at high reaction temperature, from $\mathrm{R{-}OH}$ to $\mathrm{R{-}O^-} + \mathrm{H^+}$. The $\mathrm{R{-}O^-}$ coordinates with the $\mathrm{Fe^{2+}/Fe^{3+}}$ of the $\mathrm{Fe_3O_4}$ nanoparticle while the $\mathrm{H^+}$ associates with the particles along with the $\mathrm{R{-}O^-}$ and as a consequence surface of the nanoparticles becomes positively charged. This, the adsorbed $\mathrm{R{-}O^-}$ and the associated $\mathrm{H^+}$ ions

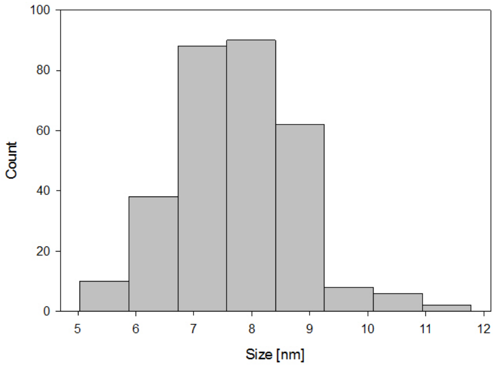

Figure 4.6: Particle size distribution of IONPs prepared by Fe(acac)$_3$ in presence of TREG (8±1 nm)

cause the steric and electrostatic interactions between the nanoparticles.

The lower zeta potential for the first batches could therefore indicate that there were still some excess surfactant that was left in the sample, which was reduced when increaing the number of washing steps. It could also indicate that the nanoparticles were less stable as fewer H$^+$ ions would cause more interactions between the nanoparticles, giving rise to a larger hydrodynamic size.

A modified protocol was also carried out, where to ratio of precursor to solvent was changed from 2 mmol:20 mL to 1 mmol:30 mL. This gave hydrodynamic size at 172 ± 6 nm and zeta potential at 24.3 ± 0.6 mV, which was close to the already established protocol. However, due to a small yield of nanoparticles (15 mg vs 135 mg), this method was not further investigated. For further experiments with carboxyl-functionalization, the obtained nanoparticles from the first method was coated with poly(acrylic acid).

4.1.3 Fe(acac)$_3$ + OAm

Thermal decomposition of Fe(acac)$_3$ in the presence of mixture of oleylamine (OAm) and benzyl ether was performed, and S(T)EM image of the obtained nanoparticles are shown in Figure 4.7. The particles were spherical and had an average size of 8 ± 1 nm, as seen from the particle size distribution in Figure 4.4.

In order to go further with these nanoparticles for carboxyl-functionalization by coating of poly(acrylic acid), the particles had to be phase transferred as the hydrophobic as-prepared particles were dissolved in toluene. It was chosen to try a base-bath-assisted phase transfer, as previously reported by *V. Vilas-Boas et al.*

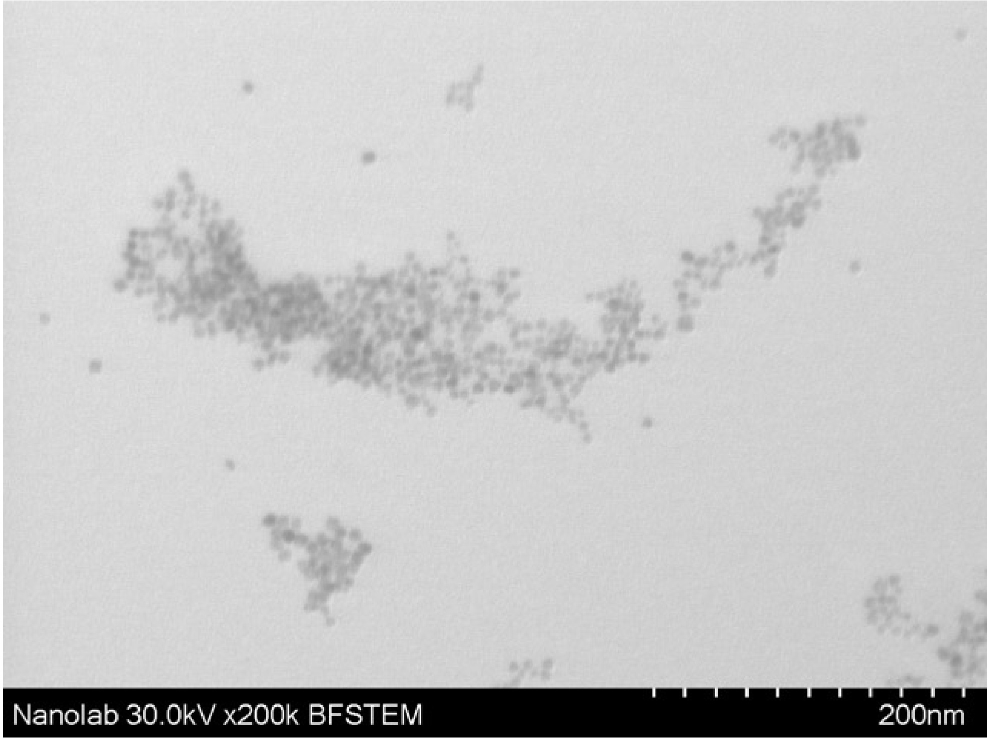

Figure 4.7: BF S(T)EM image of IONPs synthesized by Fe(acac)$_3$ + OAm/BE·

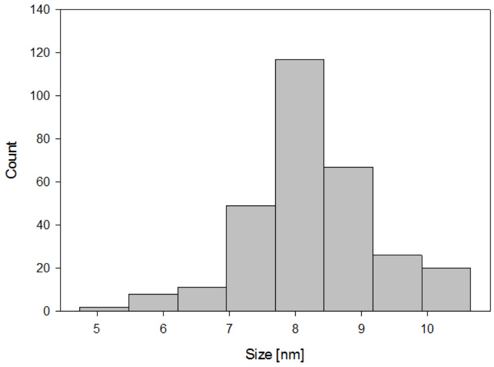

Figure 4.8: Particle size distribution of IONPs prepared by Fe(acac)$_3$ in presence of OAm and BE (8±1 nm)

[22] The base used was potassium hydroxide (KOH), that was dissolved in a 50:50 mixture of water and isopropanol. This was then added to a dispersion of IONPs, and the mixture was sonicated for 30 min with brief vortexing in between. The pictures in Figure 4.9 shows how the IONPs in the upper organic layer transitioned to the bottom aqueous layer, indicating that the phase transfer was successful.

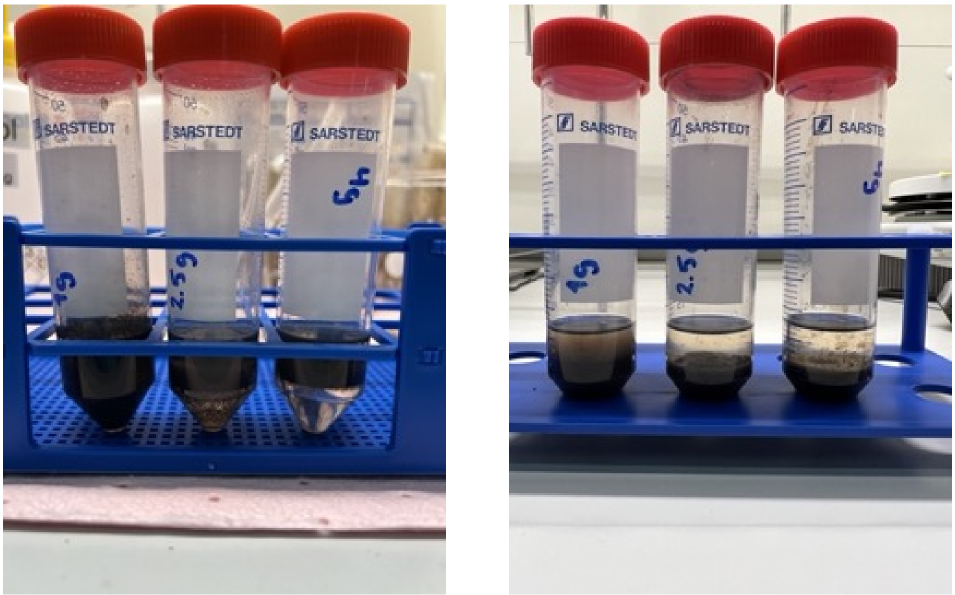

Figure 4.9: Base-bath-assisted phase transfer of IONPs. Image to the left is taken before sonication, and the one to the right is after 30 min of sonication and 24 hours of shaking.

In the work of *V. Vilas-Boas et al.* the phase transfer was carried out for oleate-capped IONPs synthesized by thermal decomposition of iron oleate. Further literature review revealed no such examples of applying this specific phase transfer for OAm capped IONPs. It was therefore necessary to do some investigation on how the reaction parameters effected the final hydrodynamic size and zeta potential of the as-transferred IONPs. Firstly, it was looked into how the amount of KOH in the base-bath solution affected the mentioned properties. This was measured by DLS, and measurements were carried out in the same way as for the IONPs prepared by $Fe(acac)_3$ + TREG. From the results given in Table 4.2, it was observed that the higher the amount of KOH the lower sizes. The zeta potential however did not reveal any such trend.

It was also studied how the time duration of the shaking after the sonication affected the hydrodynamic size and zeta potential. For this experiment the IONPs

Amount of KOH	Hydrodynamic size [nm]	Polydispersity index [%]	Zeta potential [mV]
1g	730 ± 155	27 ± 0	18.5 ± 0.5
2.5g	405 ± 1	26 ± 1	20.3 ± 0.7
4g	344 ± 11	28 ± 5	15.7 ± 0.4

Table 4.2: Mean values with corresponding standard deviation from DLS measurements for samples with varying amount of KOH. Each samples were measured in triplicates, and for hydrodynamic size and polydispersity index each measurements consisted of 10 runs à 10 seconds, whereas for measurements of zeta potential consisted of 100 runs.

was dispersed in toluene, whereas for the previous one they were dispersed in cyclohexane according to the method of *V. Vilas-Boas et al.* As the OAm-capped nanoparticles were stored in toluene, it was therefore of interest to investigate whether if it was necessary to have the nanoparticles dispersed in cyclohexane when performing the phase transfer or not. In addition, another study that employed a modified method of this phase transfer had also used toluene instead of cyclohexane. [25] From the plots given in Figure 4.10 it can be seen that the trend for the size was that a longer shaking time gave smaller nanoparticles, and there was a slight increase in zeta potential from no shaking up to four hours where it stabilized around 24.5 mV. Based on these results, it was concluded that the optimal protocol for getting hydrophilic nanoparticles with a small size was to add 4 g of KOH in the base-bath mixture and shake the solution for 24 hours after sonication.

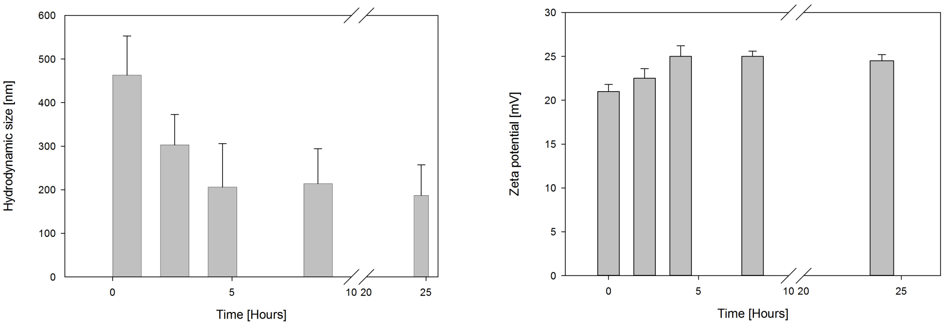

Figure 4.10: Hydrodynamic size and zeta potential with corresponding standard deviation from the time-based study of base-bath-assisted phase transfer.

The authors of the paper hypothesized that the strong base, KOH, would eliminate the organic capping and stabilization of the IONPs was caused by ionic sta-

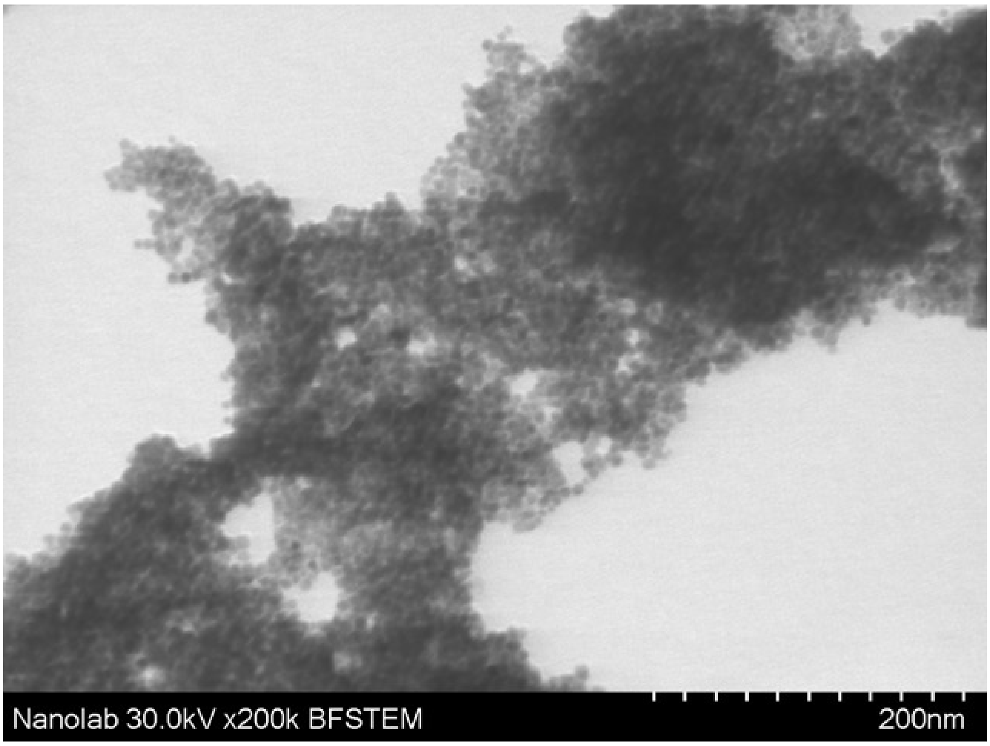

Figure 4.11: BF S(T)EM image of the IONPs prepared by $Fe(acac)_3$ + OAm/BE after base-bath-assisted phase transfer.

bilization of negatively charge $Fe-O^-$ surface species. The results from the experiments in this thesis shows that a more alkaline solution and longer reaction time led to formation of smaller nanoparticles, suggesting that the base in fact etched away the organic coating. However, the positive zeta potential at around 25 mV (pH 9.6) was not coherent with negative zeta potential of -89 mv (pH 9) that was observed in the work of *V. Vilas-Boas et al.* [22] This is hypothesized to be explained by the different nature of the nanoparticles. Where the original work used oleic acid as capping ligand, oleylamine was employed for this experiment. Previous studies has shown that at $pH > 7.4$ the zeta potential is positive for oleylamine, as the NH_2 group protonates to ${NH_3}^+$. [26] It was therefore concluded that the base-bath partially stripped away the organic capping, making the nanoparticles dispersible in water, but there were still some oleylamine remaining on the surface. In Figure 4.11 a S(T)EM image of the phase transferred IONPs is shown. It is observed that the particles remained spherical even after phase transfer.

4.1.4 $Fe(acac)_3$ + OA

Cubic shaped IONPs were prepared by thermal decomposition of iron acetylacetonate ($Fe(acac)_3$) in benzyl ether with oleic acid (OA) as surfactant. S(T)EM image of the obtained nanoparticles is shown in Figure 4.12, from which it can be concluded that cubic shape was in fact achieved. The mean length of the sides was 86 nm ±11 nm, and the size distribution is given in Figure 4.13. This is not consistent with previously reported experiments with similar reaction conditions. *Singh et al.* reported cubic shaped IONPs with an average size of 26 nm with a standard deviation of 9%. [20] Not only is the sizes much lower, but the uniformity or monodispersity is enhanced. However, it was reported that as the reaction time was prolonged up to 60 minutes the size increased to approximately 40 nm. This growth can be attributed to an Ostwald ripening process, where smaller nanoparticles with high surface energy would redissolve and contribute to growth on larger nanoparticles with lower surface energy.

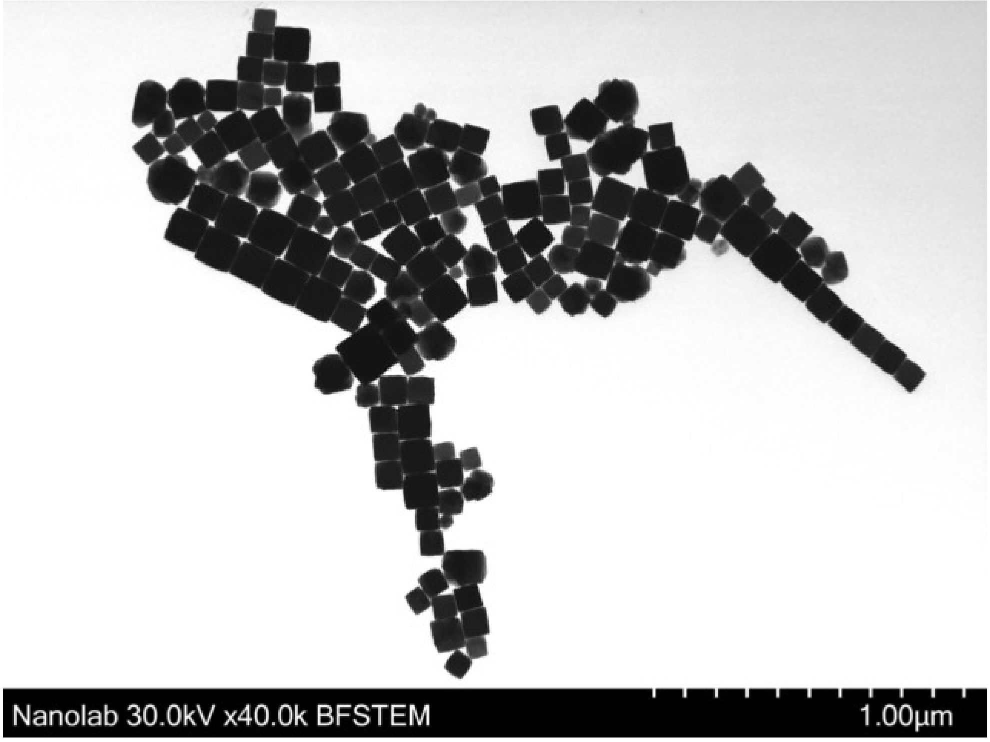

Figure 4.12: S(T)EM image of cubic shaped IONPs prepared by thermal decomposition of $Fe(acac)_3$ + OA

Singh et al. also reported the formation of cubic nanoparticles with an aver-

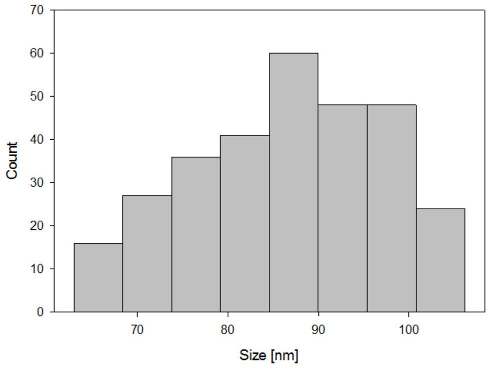

Figure 4.13: Particle size distribution of IONPs prepared by Fe(acac)$_3$ in presence of OA (86±11nm)

age size of 85 nm, which was achieved by changing the heating rate from the degassing temperature up to the final reaction temperature from 20 °/min down to 3 °/min. [20] This change led to a different supersaturation profile. A slow heating rate would lead multiple nucleation events occurring at different time intervals, and the nucleation and growth processes would not be clearly separated. Employing a more rapid heating rate would yield a more burst nucleation leading to a formation of large number of nuclei which consumes much of the available monomers, leaving a low concentration of monomers available to contribute in the growth process of the formed nuclei. Based on this it can be hypothesized that the reason behind the formation of larger nanoparticles for this project compared to the ones reported by *Singh et al.* is the supersaturation build up with a more sluggish nucleation rate yielding larger sized nanoparticles. However, it is unlikely that the heating rate is the reason behind the large deviation, as the temperature profile was regulated by the PID controller and closely monitored during the synthesis and was in fact determined to be 20 °C/min.

The synthesis was performed using a vacuum pump during the degassing stage, in order to control the residual pressure or the remaining oxygen content in the reaction environment. One reason that it was desirable to operate with vacuum conditions was due to the fact that given a sufficient amount of oxygen present in the system is hypothesized to induce a decomposition of benzyl ether, which was used as the solvent. At normal conditions benzyl ether would decompose at temperatures between 310 and 350 °C, but the presence of an acid could catalyze the decomposition to occur at lower temperatures eventually leading to the formation of toluene (bp = 110 °C) and benzaldehyde (bp = 178 °C). [27] *Guardia et al.* demonstrated the effect of the simultaneous decomposition of benzyl ether along with the decomposition of Fe(acac)$_3$ in the presence of decanoic acid. [28] During the synthesis a temperature decay from the reflux temperature at 295 °C down to 260-270 °was reported, along with temperature fluctuation down to 250 °C. Replacing benzyl ether with squalene improved the temperature decay somewhat as well as reducing the temperature fluctuations. However, by degassing the solvent and the reaction environment at vacuum has shown to improve this issue. [29] [20] For the syntheses performed for this project the reflux temperature was kept constant at 290 °C.

The other reason for controlling the residual oxygen content is that this parameter has shown to have an effect on both the shape and size of nanoparticles. [20] [14] In the paper from which the method is extracted, the pressure at which the reaction environment was degassed was 0.19 mbar. When increasing the degassing pressure to 0.40 mbar and 0.71 mbar truncated cubic and truncated octahedra were obtained. However, the size were not significantly different. For this project the pressure that was used for degassing was set to 0.02 mbar. The reason for the difference in employed pressure was that when setting the pressure to 0.19 mbar, cubic shaped nanoparticles could not be obtained. Instead truncated octahedra was observed, as shown in Figure 4.14. This can give an explanation to why it wasn't possible to reproduce the results of *Singh et al.*

In a paper by *G. Muscas et al.* it was demonstrated how the control of oxygen content in the reaction environment could increase the size of cobalt ferrite nanoparticles by decreasing the degassing pressure from 13.6 nm at 0.8 mbar to 18.1 nm at 0.3 mbar. [14] It was hypothesized that by reducing the oxygen content the separation between the nucleation and growth processes could be controlled. By lowering the oxygen content the nucleation event would be prolonged, leading to lower formation of nuclei compared to a quick nucleation as was described by *Singh et al*. The growth process would then occur simultaneously with the nucleation and induce a defocusing effect where particles with a broad size distribution would be formed, which later would experience a self-focusing effect due to Ostwald ripening.

Since the synthesis performed in this project took place at a lower degassing pressure than the one from which the method is extracted, it is hypothesized that this is the main reason for not being able to reproduce the work of *Singh* *et al*. However, when a second synthesis with the same reaction parameters was performed cubic nanoparticles with an average size of 86.2 nm $\pm 10,8$nm and polydispersity index of 1.6% was obtained. It can therefore be concluded that the synthesis is somewhat reproducible.

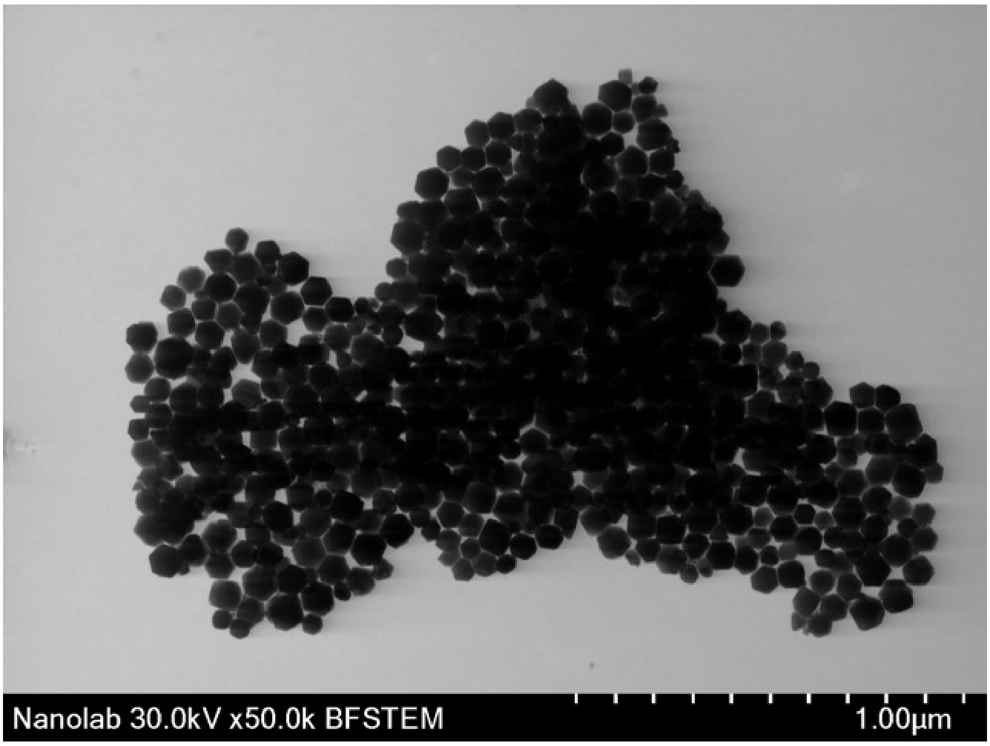

Figure 4.14: Degassing pressure at 0.19 mbar

The as-prepared IONPs was hydrophobic due to organic capping of oleic acid. In order to use them further for the biological application it was necessary to make them hydrophilic by phase transfer. For this purpose it was chosen to try the phase transfer at which $KMnO_4$ oxidizes the oleic acid ligands, providing free carboxyl groups on the surface and thereby making the nanoparticles dispersible in water.

In Table 4.3 an overview of the results from the initial experiment is listed. It can be observed that the nanoparticles had very large hydrodynamic radius and that there was a large standard deviation for the three runs. This was a clear indication that the IONPs were not successfully phase transferred. It was speculated that the amount of IONPs was too high and that it would be necessary to repeat the experiment with varying amounts of IONPs, keeping the other reaction parameters constant. An experiment where 25mg, 50 mg and 75 mg of IONPs was added was carried out. The results can be seen in Table 4.4. It was observed that regardless of the amount the nanoparticles would have a hydrodynamic size in the micron range.

	Hydrodynamic radius [nm]	Polydispersity index [%]	Zeta potential [mV]
1st series	2386	24	-29.4
2nd series	1545	28	-28.7
3rd series	2307	31	-29.4
Average	2079 ± 465	28 ± 4	-29.2 ± 0.4

Table 4.3: Results from DLS of the initial experiment of $KMnO_4$ phase transfer. Each series consisted of ten runs à ten seconds.

	Hydrodynamic radius [nm]	Polydispersity index [%]	Zeta potential [mV]
25 mg	8059 ± 1663	28 ± 9	-37.2 ± 0.4
50 mg	3909 ± 1158	29 ± 6	-23.1 ± 0.1
75 mg	5852 ± 1945	27 ± 7	-20.4 ± 0.4

Table 4.4: Results from DLS of the experiment of $KMnO_4$ phase transfer with varying amount of IONPs. Each sample were measured in triplicates consisting of ten runs à ten seconds.

As a last experiment, it was investigated how the pH of the system affected the stability of the IONPs in solution. The results from DLS are listed in Table 4.5. However, it was not possible to obtain particles with reasonable sizes.

For all the samples that was prepared it was observed that the particles would start settling within few seconds after being sonicated, which support the fact that the nanoparticles was not successfully phase transferred. It was therefore concluded that both the synthesis of the IONPs and the phase transfer method had to be further investigated and optimized. However, it was not chosen to go further with this for the time being.

4.1.5 $Fe(acac)_3$ + OA/OAm/HDD

After the phase transfer of the cubic IONPs prepared by thermal decomposition of $Fe(acac)_3$ and oleic acid in benzyl ether did not give the desirable outcome, it was proposed that a another method yielding cubic shaped IONPs was tested.

pH	Hydrodynamic radius [nm]	Zeta potential [mV]
2	3889 ±1133	28.8 ±1.1
3.5	3170± 368	16.9 ±0.4
5	3079 ±485	6.9± 0.2
7	4169± 599	-26.8 ±0.6
9	5852.2 ± 1945.1	-20.4 ±0.4
12	5084± 1604	-12.4± 0.4

Table 4.5: Results from DLS of IONPs phase transferred with $KMnO_4$ at different pH levels. Each sample were measured in triplicates consisting of ten runs à ten seconds.

Based on the work of *H. Yang et al.* a similar method was carried out. [21] What differed from the previous method was the additional use of oleylamine and 1,2-hexadecandiol, in addition to a different ratio of precursor to oleic acid. In the previous method the reatio between $Fe(acac)_3$ to oleic acid was 1:2, whereas from this particular method it was 1:16. There was also a different temperature profile for the synthesis. Whereas the previous would go right up to the decomposition temperature at 290 °C after degassing, an intermediate stage at 200 °C for 30 minutes was employed before bringing the system up to reflux.

S(T)EM image of the obtained particles are shown in Figure 4.15. From this it can be observed that the shape of the particles were not well-defined for the entire population, with presence of both cubic shaped and truncated octahedra. After performing an image analysis the average size was determined to be 12 nm ±1 nm. Particle size distribution is given in Figure 4.16. So the uniformity regarding size was hereby improved, but the shape control was of poor quality. The exact reason for this is not known, but there could be several explanation.

In the work published by *H. Yang et al.* the role of the reagents were not discussed. However, 1,2-hexadecanediol is often said to function as a reduction agent. [30] Previous studies have shown that the absence of the diol in similar systems containing both oleic acid and oleylamine, would yield large Wüstite phase particles. [31] On the contrary, the addition would suppress the growth of particles larger than 20 nm by promotion of the nucleation number. [32] This could explain the large decrease in size from the method were only oleic acid was used as reducing agent. Assuming that 1,2-hexadecanediol was mainly working as reducing

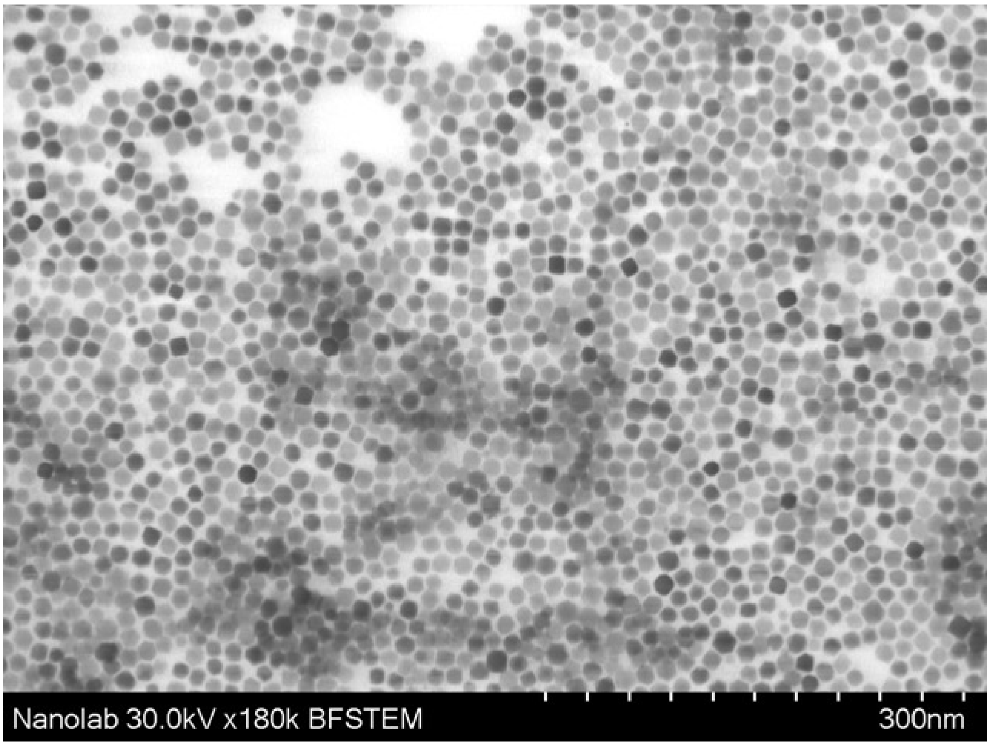

Figure 4.15: BF S(T)EM images of IONPs synthesized by Fe(acac)$_3$ in presence of OA, OAm and HDD.

agent, oleic acid and oleylamine would be considered as stabilizers and surfactants, and responsible for the shape evolution.

In this project it has been conducted experiments where both oleic acid and oleylamine has acted as surfactants alone using Fe(acac)$_3$ as precursor and benzyl ether as solvent. The former gave cubic shaped nanoparticles, whereas the latter gave spherical-like. From this it can be concluded that the surfactants binds differently to the surface and give rise to different morphologies. Oleic acid would have a selective binding to differing energy crystal facets with its carboxylic group with a nonpolar tail group for steric hindering, while oleylamine with a -NH$_2$ group has a rather weak and isotropic binding onto the surface of particles. [21] When taking the binding energy into account, it has been reported that a ratio of oleic acid:oleylamine at 4 has a binding energy of appox -6500 kcal/mole compared to approx -3000 kcal/mole for oleic acid only. [33] It is therefore reasonable to assume that both oleic acid and oleylamine were bound to the surface of the obtained properties as this would yield more stabile nanoparticles, which could ex-

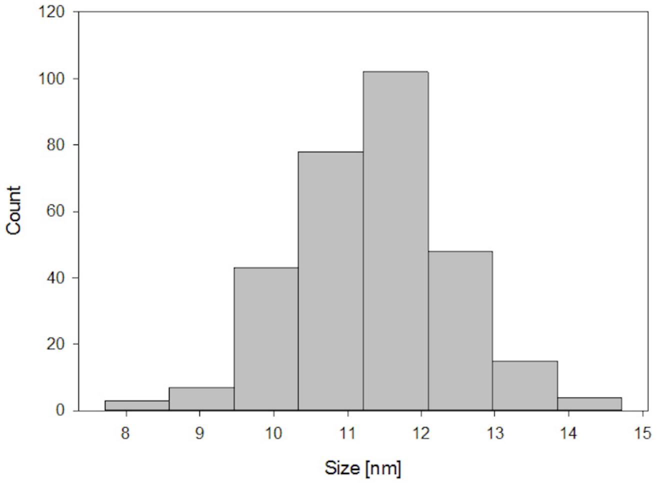

Figure 4.16: Particle size distribution of IONPs synthesized by Fe(acac)$_3$ in presence of OA, OAm and HDD (12±1 nm).

plain the different morphologies.

It was not stated in the published work whether the degassing step was carried out under vacuum or not. The experiment was therefore carried out without the use of a vacuum pump unlike the previous method which gave cubic shaped nanoparticles for the entire population. The presence of oxygen species at higher pressure is known to modify the surface energy of crystal facets, as the oxygen would adsorb to the {111} plane as this has a higher cationic charge than the {110} and {100} planes. Consequently the growth in the <111> plane would be suppressed, leading to truncated octahedron shape possessing both (100) and (110) facets. [20]

Regardless of the uneven shapes, it was desirable to see if the phase transfer method using KMnO$_4$ gave better results. DLS measurements revealed hydrodynamic size of 237 ± 9 nm and polydispersity index of 26% ± 1%. The zeta potential was at -37.2 ± 0.3 mV, which was close to the values at approximately -40 mV reported by *J. Cai et al.* that developed this method. [23] As nanoparticles with a zeta potential greater than 25 mV, positive or negative, usually have a high degree of stability, this could indicate that the phase transfer were indeed successful. [34] However, zeta potential and overall stability has also shown to have non correlation, and the most visual stable solution had the lowest zeta potential. [35] By observing the sample over time, it was not visually noticed any large aggregates depositing in the sample as was the case for the one method were only

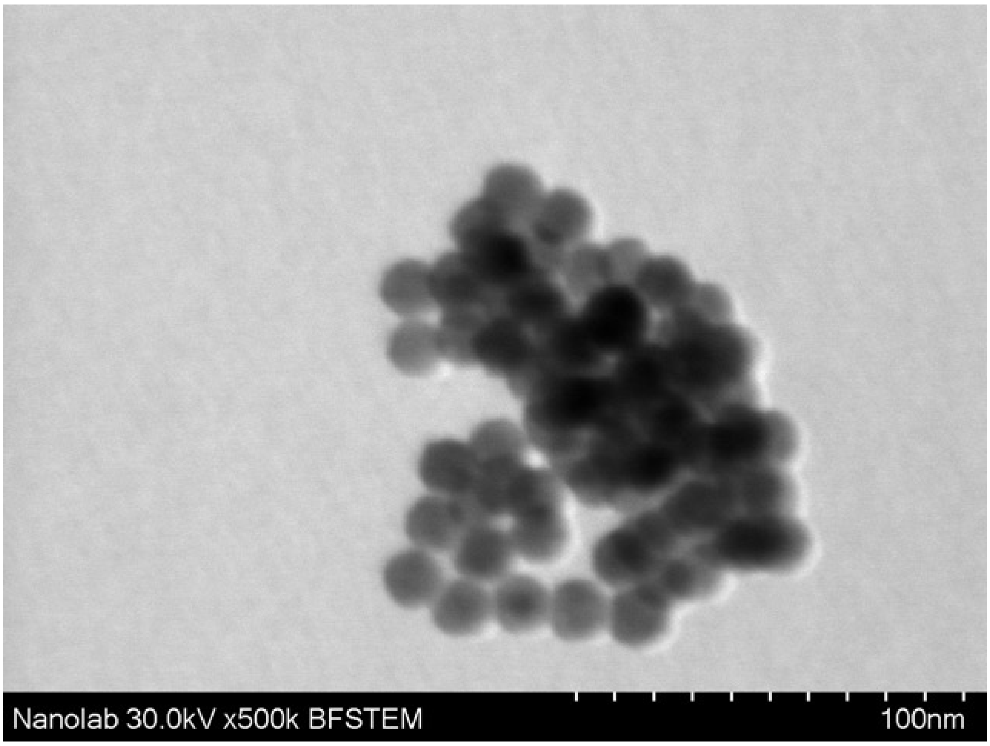

Figure 4.17: BF S(T)EM image of IONPs synthesized by FeOleate and OA.

oleic acid was used as surfactant. Also, the size of the nanoparticles resembled somewhat the sizes of the hydrophilic nanoparticles prepared in the presence of TREG. It was therefore reasonable to conclude that the phase transfer was indeed succesful and the nanoparticles were carboxyl-functionalized.

4.1.6 FeOleate + OA

Spherical OA-capped IONPs with a size of 15 ± 1 nm was synthesized by thermal decomposition of iron oleate. S(T)EM image of the obtained IONPs are given in Figure 4.17, and the particle size distribution is given in Figure 4.18. These were carboxyl-functionalized by the same method as the cubic-shaped nanoparticles, by using $KMnO_4$. DLS measurement was carried out for the sample with three series consisting of ten runs à ten seconds. The average hydrodynamic size was 196 nm with a standard deviation of 18 nm and a polydispersity index of 28±2%. The zeta potential was highly negative with -50 ± 0 mV, which originated from the deprotonated carboxylic groups.

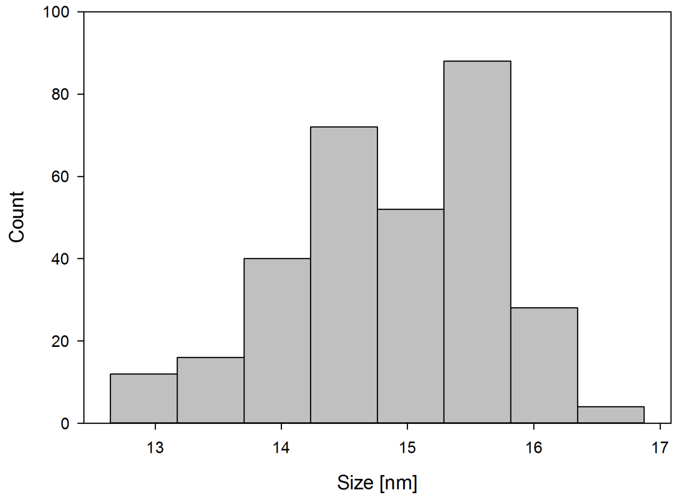

Figure 4.18: Particle size distribution of IONPs synthesized by Feoleate and OA (15±1nm).

4.2 PAA coating

For the samples that were not phase transferred using $KMnO_4$, carboxyl-functionalization was achieved by coating the nanoparticles with poly(acrylic acid) (PAA). Initial experiment was carried out following the protocol developed for IONPs synthesized by coprecipitation. This resulted in large nanoparticles in micron-range according to DLS measurements and the size distribution was uneven for multiple runs, as seen in Figure 4.19. It was also observed a great offset for the intensity correlation function, g_2, at the end of the graph, which indicated aggregation of nanoparticles in the solution. This zeta potential was at -18.9 ± 0.6 mV, which was lower than what is usually observed for PAA-coated nanoparticles ($\approx$ -25 mV). In sum, it was concluded that these nanoparticles was unstable and the method had to be changed for thermal decomposition nanoparticles. As it was observed a strong orange color of the supernatant after the reaction was done, it was hypothesized that the amount of monomer (AA) to IONPs was too high. The amount of IONPs was therefore increased to twice the amount of IONPs used in the initial experiment, which resulted in more stable nanoparticles with smaller sizes and zeta potential close to expected values. Results from DLS measurements of these particles are reported in Table 4.6.

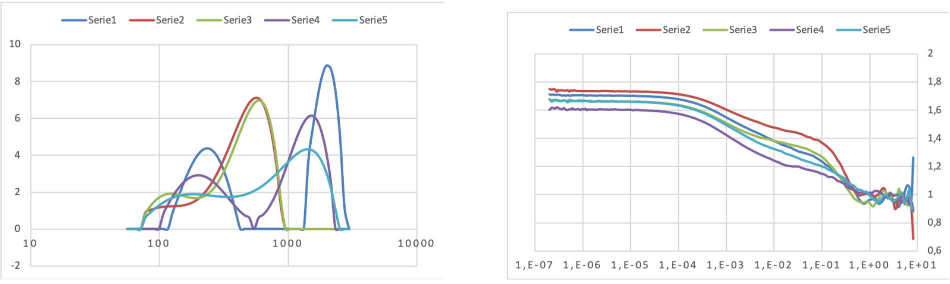

Figure 4.19: Results from DLS measurements of initial experiment of PAA-coating, with size distribution (left) and intensity correlation function (right).

Sample	Hydrodynamic size [nm]	Polydispersity index [%]	Zeta potential [mV]
PAA@[Fe(acac)3 + TREG]	767 ± 16	36 ± 2	-26.2 ± 0.17
PAA@[Fe(acac)3 + OAm]	403 ± 1	24 ± 1	-24.4 ± 0.4

Table 4.6: Results from DLS measurements of PAA-coated IONPs. Each sample was measured in triplicates consiting of 10 runs à 10 seconds.

4.3 Quantification of Carboxyl Groups on the Surface of NPs

In order to determine the quantity of carboxylic groups on the surface of NPs, a colorimetric method reported by *A. Hennig et al.* was carried out. [24] In short terms, $NiCl_2$ is added to the sample of interest along with pyrocatechol violet (PV). Ni_2^+ ions would then bind to the carboxylic groups on IONPs, and assuming that the bound ion corresponds to 2.65 carboxylic groups, the number of carboxylic groups can be quantified by determining the remaining concentration of free nickel ions in the solution. UV-vis is employed to detect free nickel-ions.

Sample	COOH on the NPs [mmol/g], 0.2 mg	COOH on the NPs [mmol/g], 0.4 mg	COOH on the NPs [mmol/g], average
PAA@[Fe(acac)$_3$ + OAm]	1.49 ± 0.00	1.00 ± 0.06	1.24 ± 0.27
PAA@[Fe(acac)$_3$ + TREG]	0.88 ± 0.02	0.67 ± 0.03	0.77 ± 0.12
FeOleate + OA	0.47 ± 0.05	0.37 ± 0.04	0.42 ± 0.06
Fe(acac)$_3$ + OA/OAm/HDD	0.44 ± 0.04	0.32 ± 0.00	0.37 ± 0.07

Table 4.7: Results from COOH quantification

Based on the conducted experiment, it can be concluded that the coating procedure with PAA gives a higher amount of carboxylic groups than reducing the oleic acid ligands.

4.4 Magnetic strength

The saturation magnetization of the samples prepared was measured by vibrating sample magnetometer (VSM). In Table 4.8 and 4.9 the values for the as-prepared IONPs and carboxyl-functionalized IONPs are presented, respectively. The hysteresis loops for the carboxyl-functionalized IONPs are shown in Figure 4.20.

Sample	M_s **[emu/g]**
Fe(acac)$_3$ + TREG	60
Fe(acac)$_3$ + OAm/BE	66
KOH p.t. Fe(acac)$_3$ + OAm/BE	57
Fe(acac)$_3$ + OA/OAm/HDD	79
FeOleate + OA	29

Table 4.8: Overview of saturation magnetization for as-prepared IONPs.

Sample	M_s **[emu/g]**
PAA@Fe(acac)$_3$ + TREG	58
PAA@Fe(acac)$_3$ + OAm/BE	52
Fe(acac)$_3$ + OA/OAm/HDD	76
FeOleate + OA	17

Table 4.9: Overview of saturation magnetization for carboxyl-functionalized IONPs.

For the TREG-capped IONPs there is a small drop in saturation magnetization from the as-prepared IONPs to the PAA-coated. This is consistent with previous findings of PAA-coated IONPs prepared by co-precipitation. Whereas for the PAA-coated OAm/BE-capped IONPs a larger decrease is observed. This is partially explained by the phase transfer, as this led to a reduction of magnetic strength. However, the difference in saturation magnetization between the two PAA-coated IONPs could be seen in relation to findings from the quantification of carboxylic groups on the surface. The PAA@Fe(acac)$_3$ + OAm/BE were found to have a larger number of COOH groups, which could shield the magnetic core in a greater extent.

The cubic IONPs prepared by Fe(acac)$_3$ + OA/OAm/HDD showed high satur-

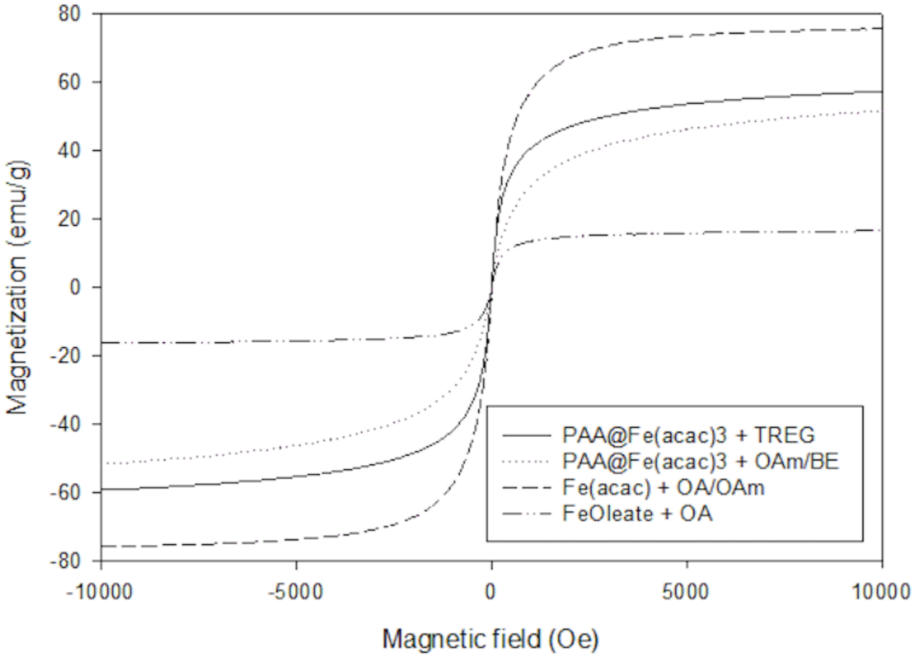

Figure 4.20: Hysteresis loops for carboxyl-functionalized IONPs.

ation magnetization both before and after phase transfer. This could be attributed to the fact that after the phase transfer there is a lower organic content since the oleic acid-ligand has been reduced, which leads to the particles being able to maintain the magnetic properties. However, this was not observed for the iron oleate nanoparticles, which experienced a drop of saturation magnetization at almost 50%. It was observed after the phase transfer that the magnetic separation of nanoparticles diminished during the washing steps. Eventually centrifugation was found to be more efficient in order to extract nanoparticles. By reducing the number of washing steps, the magnetic strength could have been improved. At the same time, this enhances the risk of having residual reagents left in the sample.

4.5 Biological application

The carboxyl-functionalized IONPs were sent to Erlend Ravlo at the Department of Clinical and Molecular Medicine (IKOM, NTNU) to test the performance of the IONPs in nucleic acid extraction. The nucleic acid that was to be extracted was corresponding to the Sars-CoV-2 virus. In Table 4.10 the results from qPCR test run on eluate of the samples are presented. The values listed are the average C_q numbers from the different dilution of the virus. The C_q number, or quantification cycle, is the number of cycles that were run in order to have enough copies of nucleic acid so that detection was possible and qPCR test was classified as positive. Hence, lower C_q value is preferred. The two samples listed first, 1 eq. PAA and 2 eq. PAA, were PAA-coated IONPs synthesized by coprecipitation from an earlier project. The former was synthesized as according to the method, whereas the latter had twice the amount of monomer added during the coating procedure.

Sample	1:1	1:10	1:100	1:1000
1 eq. PAA	22.29 ± 0.14	25.47 ± 0.09	28.59 ± 0.45	31.68 ± 0.26
2 eq. PAA	22.62 ± 0.22	25.84 ± 0.19	28.67 ± 0.68	31.90 ± 0.19
PAA@[Fe(acac)3 + TREG]	22.83 ± 0.27	26.17 ± 0.44	29.55 ± 0.30	32.39 ± 0.41
PAA@[Fe(acac)3 + OAm]	21.82 ± 0.12	25.14 ± 0.02	28.43 ± 0.04	31.33 ± 0.10
FeOleate + OA	22.84 ± 0.55	26.03 ± 0.24	29.07 ± 0.65	31.97 ± 0.09
Fe(acac)3 + OA/OAm/HDD	21.97 ± 0.18	25.26 ± 0.03	28.44 ± 0.24	31.37 ± 0.13

Table 4.10: Overview of the number of quantitation cycles for functionalized IONPs. Each sample was run in triplicates, and the values listed are mean values with corresponding standard deviation.

It was observed that all of the functionalized IONPs managed to extract nucleic acid, as every sample was positive. The lowest C_q values were observed for the PAA-coated IONPs synthesized by $Fe(acac)_3$ + OAm and the $KMno_4$ phase transferred cubic nanoparticles, and in general they performed slightly better than the PAA coated IONPs prepared by coprecipitation. Compared to number of carboxylic groups that were quantified on the surface of the particles, these are the ones with the highest and lowest number, respectively. Meaning that there are no obvious correlation between the amount of carboxylic groups and ability to extract nucleic acids. That said, these are synthesized by different methods, and in order to conclude on the correlation equally synthesized IONPs with varying amount of carboxylic groups must be tested. However, it can be observed that the IONPs prepared with 1 equivalent of AA performed better than the one with 2 equivalent. But the number of carboxylic groups were not quantified for these, and it relies on the assumption that more monomer added in the reaction leads to a higher amount. Another interesting finding is that both the method for carboxyl-functionalization gave well performing IONPs.

Chapter 5

Final remarks

5.1 Conclusion

In this study, iron oxide nanoparticles (IONPs) were synthesized by thermal decomposition. Several different syntheses were performed using three of the most common precursors, namely iron pentacarbonyl ($Fe(CO)_5$, iron oleate (FeOleate) and iron acetylacetonate ($Fe(acac)_3$. Depending on the choice of surfactant and solvent used in the synthesis, nanoparticles with different properties were obtained.

For the thermal decomposition of $Fe(CO)_5$ spherical core-shell structured IONPs were synthesized both when using didecyldimethylammonium bromide (DDAB) and oleylamine (OAm) as surfactant. The sizes of the nanoparticles were found to be 16 ± 1 nm for both syntheses. One issue that had to be resolved for synthesizing DDAB-capped nanoparticles was the colloidal instability at long-term storage, meaning that the particles would aggregate and precipitate out of the solution. When decreasing the amount of surfactant added to the reaction from 1 to 0.8 mmol, the stability was improved. However, it was chosen not to go further with these IONPs for the time being.

IONPs synthesized by thermal decomposition of FeOleate and oleic acid (OA) resulted in spherical nanoparticles with sizes of 15 ± 1 nm. In order to carboxyl-functionalize these nanoparticles, a phase transfer from organic to aqueous phase was conducted using the oxidation agent $KMnO_4$. The OA capping ligand would then undergo an oxidative cleavage of the double bond, and a carboxylic end-group would be established. This phase transfer was also carried out for cubic-shaped IONPs obtained by thermal decomposition of $Fe(acac)_3$ and OA. However, these were observed to not be stable in dispersion. The method was therefore replaced by a method that used a higher amount of OA and addition of oleylamine and 1,2-hexadecanediol to the reaction mixture. Smaller IONPs (11 ± 1 nm) were obtained and successfully phase transferred.

Another phase transfer that was studied was the base-bath-assisted phase transfer using KOH. This was used for the spherical IONPs synthesized by thermal decomposition of Fe(acac)$_3$ and oleylamine. It was found that a higher amount and prolonged exposure (24 h) to the alkaline solution yielded smaller hydrophilic nanoparticles as the base stripped off the organic coating. However, the positive zeta potential that was measured for these particles gave rise to the hypothesis that some oleylamine remained on the surface of the nanoparticles. After phase transfer, the nanoparticles were coated with poly(acrylic acid) (PAA) which yielded free carboxylic groups on the surface. PAA-coating was also performed on spherical IONPs synthesized from thermal decomposition of Fe(acac)$_3$ and tri(ethylene glycol) (TREG).

Quantification of carboxylic groups revealed that PAA-coating resulted in the highest amount. However, when the IONPs were tested in nucleic acid extraction for detecting SARS-CoV-2, both the samples with the highest and lowest amount showed similar performance. Magnetic measurements showed that the functionalized NPs had saturation magnetization ranging from 17 to 76 emu/g, where the FeOleate NPs had the lowest and the cubic-shaped NPs had the highest. The others had magnetic properties resembling IONPs prepared by coprecipitation.

Overall, it was shown that carboxyl-functionalization of IONPs prepared by thermal decomposition fabricated good potential candidates for applications in diagnostics.

5.2 Further work

The results showed that the IONPs synthesized and functionalized in this study can perform at the same level as coprecipitated IONPs. Especially the cubic-shaped IONPs prepared by thermal decomposition of Fe(acac)$_3$ and OA, OAm and HDD were found to give promising results. It would therefore be convenient to go further with this method and perform a study where the effect of the properties of the NPs is investigated with regards to performance in biological testing. Examples of what can be done are varying amounts of surfactants used in the synthesis, which might lead to the possibility of size-tuning the IONPs. Size-tuning might also be possible by changing the temperature profile, as this would give a different supersaturation build-up.

In this study, the synthesis was carried out without the use of vacuum. By having a vacuum pump connected to the setup, one is able to control the residual pressure within the reaction environment. This was shown to be an essential part of the synthesis for another system, and it might also be transferable to this method.

Finally, it would be necessary to look into how the amount of carboxylic group affects the performance in biological testing. The cubic-shaped IONPs were carboxyl-functionalized by oxidizing the available OA-capping ligands, limiting the ability to control the amount. For further study, one such control can be possible by adding an additional coating step with PAA.

Bibliography

[1] S. Bandyopadhyay, *Fabrication and application of nanomaterials*. McGraw-Hill Education, 2019.

[2] S. Natarajan, K. Harini, G. P. Gajula, B. Sarmento, M. T. Neves-Petersen and V. Thiagarajan, 'Multifunctional magnetic iron oxide nanoparticles: Diverse synthetic approaches, surface modifications, cytotoxicity towards biomedical and industrial applications,' *BMC Mat*, vol. 1, no. 1, Dec. 2019.

[3] N. T. K. Thanh, N. Maclean and S. Mahiddine, 'Mechanisms of nucleation and growth of nanoparticles in solution,' en, *Chem. Rev.*, vol. 114, no. 15, pp. 7610–7630, Aug. 2014.

[4] S. Thomas, R. Shanks and S. Chandran, Eds., *Design and applications of nanostructured polymer blends and nanocomposite systems*, en, ser. Micro & Nano Technologies. Norwich, CT: William Andrew Publishing, Sep. 2015.

[5] J. W. Mullin, *Crystallization*, en, 4th ed. Oxford, England: Butterworth-Heinemann, May 2001.

[6] A. S. Myerson, 'Concluding remarks,' en, *Faraday Discuss.*, vol. 179, pp. 543–547, May 2015.

[7] B. D. Hamilton, J.-M. Ha, M. A. Hillmyer and M. D. Ward, 'Manipulating crystal growth and polymorphism by confinement in nanoscale crystallization chambers,' en, *Acc. Chem. Res.*, vol. 45, no. 3, pp. 414–423, Mar. 2012.

[8] J.-P. Andreassen and A. E. Lewis, 'Classical and nonclassical theories of crystal growth,' in *New Perspectives on Mineral Nucleation and Growth*, Cham: Springer International Publishing, 2017, pp. 137–154.

[9] A. Petryk, A. Giustini, P. Ryan, R. Strawbridge and P. Hoopes, 'Iron oxide nanoparticle hyperthermia and chemotherapy cancer treatment,' en, *Proc. SPIE*, vol. 7181, 71810N, Feb. 2009.

[10] X. Ma, H. Tao, K. Yang, L. Feng, L. Cheng, X. Shi, Y. Li, L. Guo and Z. Liu, ‘A functionalized graphene oxide-iron oxide nanocomposite for magnetically targeted drug delivery, photothermal therapy, and magnetic resonance imaging,’ en, *Nano Res.*, vol. 5, no. 3, pp. 199–212, Mar. 2012.

[11] A. Ali, H. Zafar, M. Zia, I. Ul Haq, A. R. Phull, J. S. Ali and A. Hussain, ‘Synthesis, characterization, applications, and challenges of iron oxide nanoparticles,’ en, *Nanotechnol. Sci. Appl.*, vol. 9, pp. 49–67, Aug. 2016.

[12] W. Wu, Z. Wu, T. Yu, C. Jiang and W.-S. Kim, ‘Recent progress on magnetic iron oxide nanoparticles: Synthesis, surface functional strategies and biomedical applications,’ en, *Sci. Technol. Adv. Mater.*, vol. 16, no. 2, p. 023 501, Apr. 2015.

[13] V. K. LaMer and R. H. Dinegar, ‘Theory, production and mechanism of formation of monodispersed hydrosols,’ en, *J. Am. Chem. Soc.*, vol. 72, no. 11, pp. 4847–4854, Nov. 1950.

[14] G. Muscas, G. Singh, W. R. Glomm, R. Mathieu, P. A. Kumar, G. Concas, E. Agostinelli and D. Peddis, ‘Tuning the size and shape of oxide nanoparticles by controlling oxygen content in the reaction environment: Morphological analysis by aspect maps,’ *Chem. Mater.*, vol. 27, no. 6, pp. 1982–1990, Mar. 2015.

[15] Y. Chen, X. Ding, Y. Zhang, A. Natalia, X. Sun, Z. Wang and H. Shao, ‘Design and synthesis of magnetic nanoparticles for biomedical diagnostics,’ en, *Quant. Imaging Med. Surg.*, vol. 8, no. 9, pp. 957–970, Oct. 2018.

[16] G. Singh, P. A. Kumar, C. Lundgren, A. T. J. van Helvoort, R. Mathieu, E. Wahlström and W. R. Glomm, ‘Tunability in crystallinity and magnetic properties of core-shell fe nanoparticles,’ *Particle & Particle Systems Characterization*, vol. 31, no. 10, pp. 1054–1059, May 2014. DOI: `10.1002/ppsc.201400032`. [Online]. Available: `https://doi.org/10.1002/ppsc.201400032`.

[17] S. Peng, C. Wang, J. Xie and S. Sun, ‘Synthesis and stabilization of monodisperse fe nanoparticles,’ *Journal of the American Chemical Society*, vol. 128, no. 33, pp. 10 676–10 677, Aug. 2006. DOI: `10.1021/ja063969h`. [Online]. Available: `https://doi.org/10.1021/ja063969h`.

[18] D. Maity, S. Kale, R. Kaul-Ghanekar, J.-M. Xue and J. Ding, 'Studies of magnetite nanoparticles synthesized by thermal decomposition of iron (III) acetylacetonate in tri(ethylene glycol),' *Journal of Magnetism and Magnetic Materials*, vol. 321, no. 19, pp. 3093–3098, Oct. 2009. DOI: `10.1016/j.jmmm.2009.05.020`. [Online]. Available: `https://doi.org/10.1016/j.jmmm.2009.05.020`.

[19] Z. Xu, C. Shen, Y. Hou, H. Gao and S. Sun, 'Oleylamine as both reducing agent and stabilizer in a facile synthesis of magnetite nanoparticles,' *Chemistry of Materials*, vol. 21, no. 9, pp. 1778–1780, Apr. 2009. DOI: `10.1021/cm802978z`. [Online]. Available: `https://doi.org/10.1021/cm802978z`.

[20] G. Singh, V. S. Myasnichenko and W. R. Glomm, 'New insights into size-controlled reproducible synthesis of anisotropic fesub3/subosub4/sub nanoparticles: The importance of the reaction environment,' *Materials Advances*, vol. 1, no. 5, pp. 1077–1082, 2020. DOI: `10.1039/d0ma00275e`. [Online]. Available: `https://doi.org/10.1039/d0ma00275e`.

[21] H. Yang, T. Ogawa, D. Hasegawa and M. Takahashi, 'Synthesis and magnetic properties of monodisperse magnetite nanocubes,' *Journal of Applied Physics*, vol. 103, no. 7, p. 07D526, Apr. 2008. DOI: `10.1063/1.2833820`. [Online]. Available: `https://doi.org/10.1063/1.2833820`.

[22] V. Vilas-Boas, N. Guldris, E. Carbó-Argibay, D. G. Stroppa, M. F. Cerqueira, B. Espiña, J. Rivas, C. Rodrıguez-Abreu and Y. V. Kolen'ko, 'Straightforward phase-transfer route to colloidal iron oxide nanoparticles for protein immobilization,' *RSC Advances*, vol. 5, no. 59, pp. 47 954–47 958, 2015. DOI: `10.1039/c5ra08200e`. [Online]. Available: `https://doi.org/10.1039/c5ra08200e`.

[23] J. Cai, Y. Q. Miao, B. Z. Yu, P. Ma, L. Li and H. M. Fan, 'Large-scale, facile transfer of oleic acid-stabilized iron oxide nanoparticles to the aqueous phase for biological applications,' *Langmuir*, vol. 33, no. 7, pp. 1662–1669, Feb. 2017. DOI: `10.1021/acs.langmuir.6b03360`. [Online]. Available: `https://doi.org/10.1021/acs.langmuir.6b03360`.

[24] A. Hennig, A. Hoffmann, H. Borcherding, T. Thiele, U. Schedler and U. Resch-Genger, 'Simple colorimetric method for quantification of surface carboxy groups on polymer particles,' *Analytical Chemistry*, vol. 83, no. 12,

pp. 4970–4974, May 2011. DOI: `10.1021/ac2007619`. [Online]. Available: `https://doi.org/10.1021/ac2007619`.

[25] O. V. Volodina and https://pnojournal.wordpress.com/2022/07/01/volodina-3/, 'Formation of future teachers' worldview culture by means of foreign-language education,' *P Sci Edu*, vol. 57, no. 3, pp. 126–159, Jul. 2022.

[26] L. Rabinovich-Guilatt, P. Couvreur, G. Lambert, D. Goldstein, S. Benita and C. Dubernet, 'Extensive surface studies help to analyse zeta potential data: The case of cationic emulsions,' *Chemistry and Physics of Lipids*, vol. 131, no. 1, pp. 1–13, Aug. 2004. DOI: `10.1016/j.chemphyslip.2004.04.003`. [Online]. Available: `https://doi.org/10.1016/j.chemphyslip.2004.04.003`.

[27] K. E. Gilbert and J. J. Gajewski, 'Coal liquefaction model studies: Free radical chain decomposition of diphenylpropane, dibenzyl ether, and phenethyl phenyl ether via .beta.-scission reactions,' *The Journal of Organic Chemistry*, vol. 47, no. 25, pp. 4899–4902, Dec. 1982. DOI: `10.1021/jo00146a016`. [Online]. Available: `https://doi.org/10.1021/jo00146a016`.

[28] P. Guardia, A. Riedinger, S. Nitti, G. Pugliese, S. Marras, A. Genovese, M. E. Materia, C. Lefevre, L. Manna and T. Pellegrino, 'One pot synthesis of monodisperse water soluble iron oxide nanocrystals with high values of the specific absorption rate,' *Journal of Materials Chemistry B*, vol. 2, no. 28, p. 4426, 2014. DOI: `10.1039/c4tb00061g`. [Online]. Available: `https://doi.org/10.1039/c4tb00061g`.

[29] B. H. McDonagh, C. Staudinger, P. S. Normile, J. A. D. Toro, S. Bandyopadhyay, W. R. Glomm and G. Singh, 'New insights into controlling the twin structure of magnetic iron oxide nanoparticles,' *Applied Materials Today*, vol. 24, p. 101 084, Sep. 2021. DOI: `10.1016/j.apmt.2021.101084`. [Online]. Available: `https://doi.org/10.1016/j.apmt.2021.101084`.

[30] M. D. Nguyen, H.-V. Tran, S. Xu and T. R. Lee, 'Fe3o4 nanoparticles: Structures, synthesis, magnetic properties, surface functionalization, and emerging applications,' *Applied Sciences*, vol. 11, no. 23, p. 11 301, Nov. 2021. DOI: `10.3390/app112311301`. [Online]. Available: `https://doi.org/10.3390/app112311301`.

[31] M. Nakaya, R. Nishida and A. Muramatsu, 'Preparation of wüstite nanoparticles by a solventless synthetic procedure,' *Chemistry Letters*, vol. 42, no. 8, pp. 863–865, Aug. 2013. DOI: `10.1246/cl.130233`. [Online]. Available: `https://doi.org/10.1246/cl.130233`.

[32] M. Nakaya, R. Nishida and A. Muramatsu, 'Size control of magnetite nanoparticles in excess ligands as a function of reaction temperature and time,' *Molecules*, vol. 19, no. 8, pp. 11 395–11 403, Aug. 2014. DOI: `10.3390/molecules190811395`. [Online]. Available: `https://doi.org/10.3390/molecules190811395`.

[33] R. A. Harris, P. M. Shumbula and H. van der Walt, 'Analysis of the interaction of surfactants oleic acid and oleylamine with iron oxide nanoparticles through molecular mechanics modeling,' *Langmuir*, vol. 31, no. 13, pp. 3934–3943, Mar. 2015. DOI: `10.1021/acs.langmuir.5b00671`. [Online]. Available: `https://doi.org/10.1021/acs.langmuir.5b00671`.

[34] A. J. Shnoudeh, I. Hamad, R. W. Abdo, L. Qadumii, A. Y. Jaber, H. S. Surchi and S. Z. Alkelany, 'Synthesis, characterization, and applications of metal nanoparticles,' in *Biomaterials and Bionanotechnology*, Elsevier, 2019, pp. 527–612. DOI: `10.1016/b978-0-12-814427-5.00015-9`. [Online]. Available: `https://doi.org/10.1016/b978-0-12-814427-5.00015-9`.

[35] I. Roland, 'Systematic characterization of oil-in-water emulsions for formulation design,' *International Journal of Pharmaceutics*, vol. 263, no. 1-2, pp. 85–94, Sep. 2003. DOI: `10.1016/s0378-5173(03)00364-8`. [Online]. Available: `https://doi.org/10.1016/s0378-5173(03)00364-8`.

Norwegian University of
Science and Technology